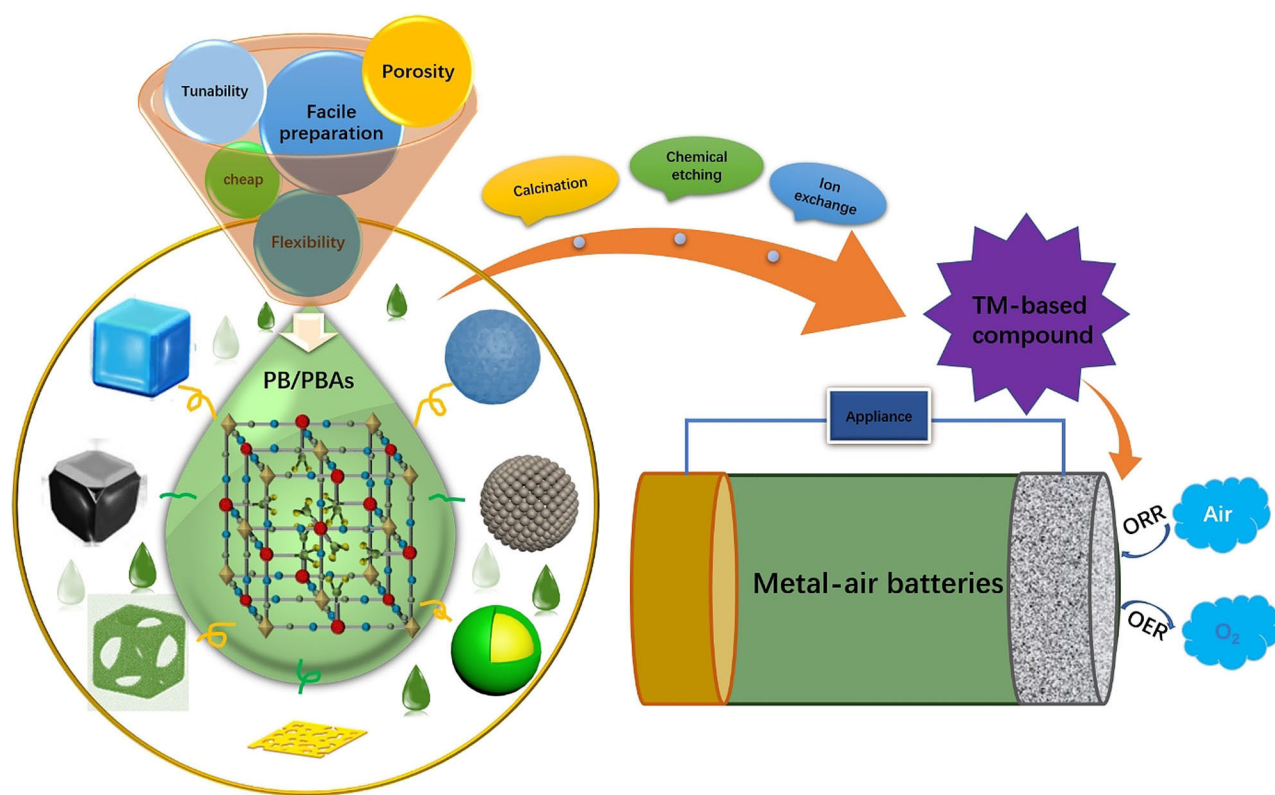


VIP Very Important Paper

Special Issue

# Functional Electrocatalysts Derived from Prussian Blue and its Analogues for Metal-Air Batteries: Progress and Prospects

Chen Deng<sup>[a]</sup> and Da-Wei Wang\*<sup>[a]</sup>

Metal-air batteries holding exceptionally high energy densities have been heavily explored recently amongst the promising next generation energy suppliers. However, their development for real application is restricted mainly due to the sluggish rates of the oxygen-reduction reaction (ORR) and oxygen-evolution reaction (OER) in the positive electrode. Thus, searching a facile way to attain highly efficient ORR and OER electrocatalysts are highly desirable. The key factors to improve the electrochemical performance of materials are to optimize their low-dimensional feature and adjust effective compositions. Prussian blue and its analogues (PB/PBAs) with open framework have attracted growing attention as hopeful precursors and templates to diverse transition metal-based materials and carbon hybrids for

ORR and OER. Compared to other precursors, PB/PBAs are more feasible for large-scale application due to their easy preparation, low cost, tuneable compositions and great environmental friendliness. In this review, recent progresses in the utilization of PB/PBA to rationally design and synthesize complex composites with controlled morphologies, sizes, and compositions for ORR, OER and metal-air batteries are described in detail. Afterwards, a brief summary of the synthetic methods to complex transition metal-based compositions with nanostructures converted from PB/PBAs are provided. Lastly, the research challenges and possible development direction of open framework materials for metal-air batteries are outlined through analysing the merits and drawbacks of using PB/PBAs as precursors.

## 1. Introduction

Nowadays, all the clean energy obtained from nature, such as solar, wind, tidal and geothermal powers, have been extensively explored to alleviate energy crisis and satisfy the energy demand of economy development.<sup>[1,2]</sup> To well balance the unpredictable energy generation and the huge energy requirement, great efforts are devoted to developing new-generation electrochemical energy storage devices which are indispensable components in the future energy network.<sup>[3–5]</sup> Lithium-ion batteries (LIBs) by virtue of high energy densities have been well developed and utilized into a myriad of applications, such as consumable electronic devices and electric transport systems.<sup>[2,6–8]</sup> Nonetheless, the radical development of electric vehicles (EVs) has urged the need of more powerful batteries.<sup>[9,10]</sup> However, the intercalation chemistry of LIBs restricts the practical specific energy,<sup>[11,12]</sup> which challenges the use of LIBs for long driving distance EVs.<sup>[13]</sup> Great efforts thus have been made to seek new alternatives to increasing the energy density of batteries.<sup>[4,13–15]</sup> Metal-air batteries thus have come into the spotlight because of their high specific energy and low manufacturing cost.

Metal-air batteries are made up of metal anode, air-breathing cathode and electrolytes, which combine the features of traditional batteries and fuel cells.<sup>[16,17]</sup> By using different metals (e.g. Zn, Fe, Al, Mg, Li, Na, K and Ca) as anode, up to now, different kinds of metal-air batteries have been extensively investigated. Their theoretical energy density ranges from  $1200\text{--}11140\text{ Wh}\cdot\text{kg}^{-1}$ , which is 3–30 times larger than that of LIBs, showing great potential for future energy applications.<sup>[18–20]</sup> Divided by electrolytes, popular Zn-air, Al-air, Fe-air and Mg-air batteries are aqueous batteries, while typical Li–O<sub>2</sub>, Na–O<sub>2</sub>, K–O<sub>2</sub> and Ca–O<sub>2</sub> are nonaqueous batteries.<sup>[13,21–22]</sup> Typically, Zn-air and Li–O<sub>2</sub> have received the most extensive

attention among all the prospective metal-air batteries. From both technical and economic aspects, Zn-air batteries possess a higher theoretical energy density of  $1086\text{ Wh}\cdot\text{kg}^{-1}$  (including oxygen) and a lower cost around  $10\text{ \$ kW}^{-1}\text{ h}^{-1}$  than that of LIBs, making it a viable alternative to replace LIBs for future EV applications.<sup>[23]</sup> In fact, the primary Zn-air battery was firstly designed in 1878 by Maiche, and its commercial products were marketed in 1932, implying the research of Zn-air battery started much earlier than 1970s of LIBs.<sup>[24]</sup> Following that, Li-air batteries were developed due to its huge theoretical energy density of  $11140\text{ Wh}\cdot\text{kg}^{-1}$ , which is close to  $12200\text{ Wh}\cdot\text{kg}^{-1}$  of gasoline.<sup>[25]</sup> Hence, metal–air batteries with large energy density become the hot topic recently as they are promising for implementation in future post-Li-ion EVs.

In spite of abundant fundamental study on those metal-air batteries, the development of meta-air batteries in practice and its output energy capacity are still obstructed by many factors, especially the air-cathodes which restrict the practical energy density and enlarge battery overpotential due to the intrinsic sluggish kinetics of oxygen-reduction reaction (ORR) and oxygen-evolution reaction (OER) during recharge.<sup>[16]</sup> Since the reaction happens at tri-phase boundary and the solid electrode is simultaneously interfaced with electrolyte and gaseous oxygen, a well-prepared cathode with proper composition and architecture is highly expected in a metal-air battery. Although platinum (Pt) and iridium/ruthenium (Ir/Ru) based materials have been recognized as the most active electrocatalysts for ORR and OER,<sup>[26]</sup> respectively, their scarcity, high-cost, and poor stability impede them from applications in large scale. Therefore, efficient and cost-effective bifunctional electrocatalysts are extremely desirable to propel the achievement of metal-air batteries. Currently, various kinds of non-precious alternative materials, such as carbon-based materials,<sup>[27]</sup> transition metal-based materials and their hybrids,<sup>[28,29]</sup> in particular transition metals supported by N-doped carbons (TMNC),<sup>[30,31]</sup> have been extensively screened for catalysing the sluggish ORR and OER owing to their low-cost and excellent electrical conductivity. Although good performance has been achieved by increasing the complexity of components and architectures, the catalysts still suffer from poor stability together with tedious preparation procedures. Thus, searching a simple and viable method or

[a] C. Deng, Dr. D.-W. Wang  
School of Chemical Engineering  
The University of New South Wales  
Sydney, NSW 2052, Australia  
E-mail: da-wei.wang@unsw.edu.au  
*An invited contribution to a Special Issue on Bifunctional Catalysts for Metal-Air Batteries*



precursor to synthesize highly efficient functional electrocatalysts with controllable construction and precise composition is urgently required.

Prussian blue (PB) which possesses three-dimensional open framework structure and rigid crystalline unit, has been investigated as a promising precursor and template used in electrocatalysis due to easy preparation and low cost. PB ( $\text{Fe}^{\text{III}}_4[\text{Fe}^{\text{II}}(\text{CN})_6]_3$ ) is an ancient pigment discovered in the 18th century and comprised of  $\text{Fe}^{3+}/\text{Fe}^{2+}$  bridged by cyano group.<sup>[32]</sup> By substituting iron element with other transition metals such as cobalt, nickel, manganese, copper and zinc, various Prussian blue analogues (PBAs) with distinct chemical compositions yet similar crystal structures can be obtained.<sup>[33]</sup> Recently, PB and PBAs have been widely studied in biosensors,<sup>[34]</sup> electrochromic displays,<sup>[35]</sup> rechargeable batteries,<sup>[36]</sup> fuel cells,<sup>[37]</sup> and electrocatalysis due to their tuneable composition, superior electrochemical and photoelectrochemical properties.<sup>[38]</sup> In this review, we will concentrate on the most recent development of PB/PBA derived materials applied in OER, ORR and metal-air batteries. Firstly, the fundamental reaction mechanism for ORR and OER are introduced. Subsequently, we will summarize various PB/PBA derived transition metal-based (oxides, hydroxides, sulfides, phosphides, carbides, alloys) materials for OER and ORR, separately. Then, we will show the progress of PB/PBA-derived bifunctional electrocatalysts used in metal-air batteries, and finally give a brief overview of the methods form PB/PBAs to different target materials, illuminating the challenges and future perspectives of ideal bifunctional electrocatalysts from open-framework materials used in metal-air batteries.

## 2. Oxygen Reaction Mechanism at Cathode in Metal-Air Batteries

For both aqueous and nonaqueous electrolytes, the overall reaction at the air cathode in metal-air batteries are ORR and

OER at discharge and charge, respectively. Typically, as shown in Figure 1, in discharging process, the metal cation is formed at anode after oxidation and the released electrons transfer to the cathode to reduce the oxygen through the external circuitry. While in charging process, the discharge products are decomposed with metal cation reduced at anode and oxygen evolved at the cathode under applied voltage. Nevertheless, the reaction mechanisms of ORR and OER vary with diverse electrolytes, cathodic materials, the concentration of oxygen species (e.g., peroxides and hydroxides) and even electrode design.<sup>[39]</sup> Besides, the kinetics of oxygen-involved reaction is rather slow due to the complicated process during discharge and charge. Thus, it is important to understand the fundamental oxygen electrochemical reactions at first and then to explore efficient oxygen electrocatalysts building a better metal-air battery system. Since recent research on metal-air batteries are mostly concentrated on Zn-air batteries and Li–O<sub>2</sub> batteries, in this section, the oxygen electrochemistry is discussed based on aqueous-electrolyte system and nonaqueous-electrolyte system.

### 2.1. ORR Mechanism

Oxygen reduction reaction as an important half reaction in metal-air battery system, especially in primary metal-air battery, has already been investigated for many years in fuel cells. This reaction includes a series of complex electron transfer reactions; thus, it is highly desirable to facilitate the reaction rate and reduce reaction overpotential. In aqueous metal-air battery system, such as Zn-air battery, the ORR mechanism may still vary with different compositions, electronic structure or experimental parameters. Typically, two possible ORR mechanisms which can be concluded as four-electron pathway and two-electron pathway have been investigated depending on different oxygen adsorption mode on the metal surface. The four-electron pathway reduction is based on a bidentate O<sub>2</sub>



**Chen Deng** is currently a PhD candidate in Chemical Engineering at the University of New South Wales, Sydney. She received her Bachelor (2013) in Pharmaceutical Engineering and Master (2016) in Chemical Engineering at Beijing Institute of Technology, China. Her research is focused on designing and synthesizing highly efficient and cost-effective electrocatalyst applied in energy related reaction, including hydrogen evolution reaction, oxygen evolution reaction, oxygen reduction reaction and biomass oxidation.



**Da-Wei Wang** is currently an Associate Professor and a Scientia Fellow in the School of Chemical Engineering, UNSW Sydney. His research interest spreads from the fundamentals of the chemistry and interface mechanisms of two-dimensional energy materials, to the development of advanced electrochemical energy devices, including supercapacitors, metal/sulfur batteries, and high-throughput electrolyzers. As a Chief Investigator, Da-Wei has attracted external funding from competitive government schemes and industrial partners. Da-Wei has contributed 2 book chapters, > 100 journal publications, 8 patents and over 20 keynote/invited presentations, which received > 15,000 citations with an H-index of 45 (Google Scholar). Da-Wei has won some prestigious awards including the Finalist of 2018 AMP Tomorrow Maker, and the 2013 Scopus Young Researcher Award in Engineering and Technology.

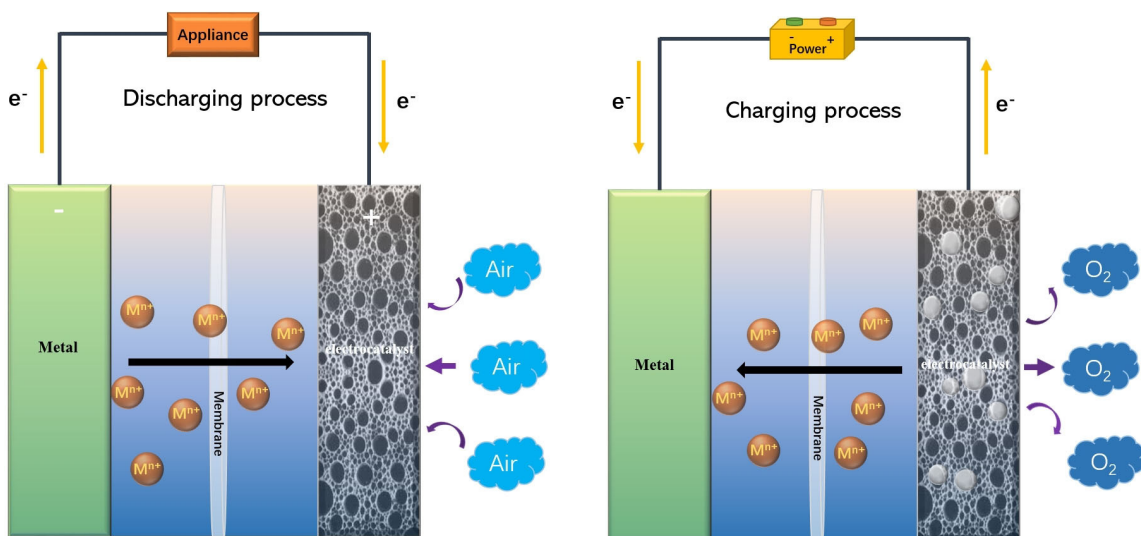
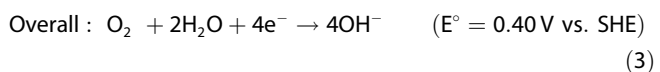
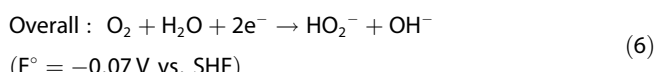
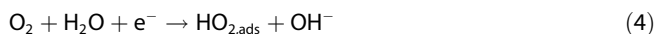


**Figure 1.** Schematic cell configurations and illustration of electrode reaction during charging and discharging process.

adsorption mode in which two O atoms are attached with catalyst simultaneously and O–O bond is subsequently weakened leading to the direct dissociation of O<sub>2</sub>, as is shown below [Eqs. (1)–(3)]:<sup>[16]</sup>



While two-electron pathway reduction is driven by end-on O<sub>2</sub> adsorption mode in which only one O atom is coordinated perpendicularly to catalyst with peroxide formation, the reactions are as follows [Eqs. (4)–(6)]:<sup>[16,19]</sup>



After two-electron reduction, the peroxide would be either reduced into hydroxide or disproportionate to oxygen. Since the HO<sub>2</sub><sup>-</sup> species will affect the efficiency and cycle stability of aqueous metal-air battery, the four-electron pathway is more desirable in ORR process owing to its high energy efficiency.<sup>[16]</sup> As for metal oxides, the general principle of ORR pathways at the surface is same, but just with a different charge distribution.<sup>[39]</sup> Usually, the four-electron pathway occurs on noble-metal based catalysts, like Pt and its alloy, whereas two-electron pathway mainly happens on carbon-based or transitional-metals based materials.<sup>[27,40]</sup> However, the two- and four-electron pathway in ORR may happen concurrently and compete with each other in reality due to the unique surface

electronic structure and electrode architecture. As is known, ORR contains complicated process with the formation of various oxygen-containing intermediates (e.g., OOH\*, OH\*, and O\*, where \* denotes a site on the electrode surface) which bind with catalyst surface differently, resulting in different rate-determining step at diverse surface. Figure 2a shows the relation between ORR activity and calculated free energy ( $\Delta E_0$ ) of the intermediates on different metal surfaces. The energy  $\Delta E_0$  closing to zero means the oxygen bonding with metal not too weak or too strong which beneficial to overall reaction. Clearly, Pt locates at the near top of the volcano plot, illustrating its best performance to ORR owing to its optimal binding to those intermediates among all candidates. However, the application of Pt in metal-air batteries will be in high cost. Herein, designing low-cost and efficient catalysts with proper binding energies to reactive intermediates is significant.<sup>[41]</sup>

Apart from the reaction in aqueous electrolyte, the ORR reaction in nonaqueous electrolyte also has been investigated, such as in Li-, Na-, and K–O<sub>2</sub> batteries. Briefly, the first step for ORR in nonaqueous electrolyte is the one electron reduction of oxygen to superoxide anion O<sub>2</sub><sup>-</sup>, and then the O<sub>2</sub><sup>-</sup> reacts with alkaline metals to form superoxide MO<sub>2</sub>. In different batteries, MO<sub>2</sub> will be further changed to peroxides due to the instability of products. Taking Li-air battery as an example, LiO<sub>2</sub> will be further decomposed into peroxide Li<sub>2</sub>O<sub>2</sub> because the small size of Li<sup>+</sup> ion makes it hard to stable O<sub>2</sub><sup>-</sup>.<sup>[15,25]</sup> In consideration of the insolubility of peroxides or superoxides, the products in metal-air batteries during discharging process will be mostly deposited on air electrode which would block the accessible surface area of active electrocatalysts gradually. Thus, it is of great importance to design proper porous structure of air-electrode to get rid of shutting off in nonaqueous metal-air batteries. Compared to the ORR in aqueous metal-air batteries, the research of ORR in nonaqueous metal-air batteries is still facing challenges that need to be overcome before their mature commercialization.

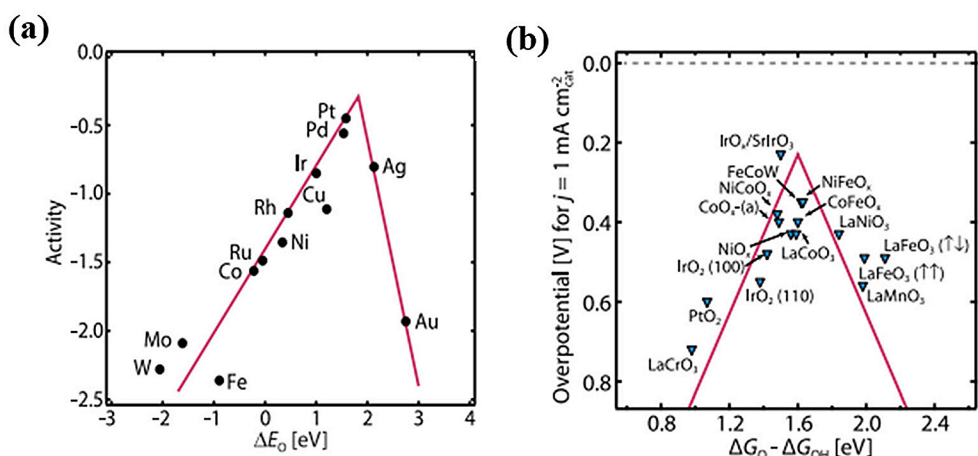


**Figure 2.** (a) ORR volcano plot for metals. (b) OER volcano plot for metal oxides.<sup>[42]</sup> Reprinted (adapted) with permission from ref. 42. Copyright (2017) Science.

## 2.2. OER Mechanism

Compared to primary metal-air battery which only involved ORR discharging process, rechargeable metal-air batteries require effective OER electrocatalyst to lower the overpotential during the charging process and increase the round-trip efficiency. Since aqueous metal-air batteries usually operate in alkaline media, here we only discuss the possible OER pathways in alkaline condition. Different from ORR, the OER mechanism possesses more complex electrochemical reactions with four discrete electron transfer steps, which are listed below [Eqs. (7)–(11)]:<sup>[16,41]</sup>



Generally, the OER is the reverse reaction of ORR pathway, and the mechanism is sensitive to various electrode materials and the surface geometry. Although many other OER mechanisms have also been proposed by numerous research groups, most of them contain same intermediates such as  $\text{OOH}^*$ ,  $\text{OH}^*$ , and  $\text{O}^*$ . The major difference among them is the last step that forms dioxygen. Thus, the binding strength of those metal-stabilized intermediates is vital to the rate-determining step and the overall OER kinetics. According to previous research, the catalysts for OER are mostly metal oxides/oxyhydroxides,<sup>[43,44]</sup> such as spinel, perovskite, rutile, and bixbyite oxides. Figure 2b shows a volcano plot containing different metal oxides and using adsorption free energy  $\Delta G_{O^*} - \Delta G_{OH^*}$  as the descriptor. As seen, the experimental overpotentials at  $1 \text{ mA cm}^{-2}$  are well consistent with the theoretical overpotential,<sup>[42]</sup> but it may not entirely reflect the intrinsic activity of materials. Some studies proposed that the intrinsic OER activity

is related to the occupancy of the 3d electron in the  $e_g$  orbital of surface metal cations, and the material with high OER activity should possess  $e_g$  occupancy close to one.<sup>[45,46]</sup>

The OER process in nonaqueous electrolyte is rather complicated. Normally, in  $\text{Li}-\text{O}_2$  batteries, the product  $\text{Li}_2\text{O}_2$  at the cathode requires high overpotential to be decomposed into  $\text{Li}^+$  and  $\text{O}_2$  due to a huge reaction barrier in charging process ( $\text{Li}_2\text{O}_2 \rightarrow 2\text{Li}^+ + \text{O}_2 + 2\text{e}^-$ ), which depresses the overall energy efficiency of Li-air batteries. In addition, the reactive intermediates, such as  $\text{O}_2^-$  and  $\text{O}_2^{2-}$ , can possibly degrade the electrolyte or electrode, resulting in poor cyclability.<sup>[47]</sup> Therefore, the nonaqueous rechargeable metal-air batteries have much more strict requirements on the electrolyte, electrode materials, oxygen pressure and device, comparing to aqueous rechargeable meta-air batteries. Much more efforts are needed to fully understand the mechanism of OER in different non-aqueous meta-air batteries. Basically, the cathode in metal air-batteries determines the final specific capacity. Searching an ideal cathode material with good intrinsic activity, conductivity, porosity and stability will benefit the charge transfer and mass transport at the interface, leading to the good battery performance. Here in this mini-review, we will focus on the structural design and composition optimization of derivatives from PB and PBAs for developing more efficient bifunctional electrocatalysts in metal-air batteries.

## 3. Electrocatalysts Derived from PB and PBA

At present, electrocatalysts can be generally divided into two categories: noble metal-based electrocatalysts and noble metal-free electrocatalysts. Among all existing catalyst systems, transition metal-carbon hybrid materials have been regarded as the most important catalysts in recent decades because of their specific characteristics, such as excellent chemical stability, tunable porosity, good electrical conductivity, excellent diversity of their structure, high specific surface area and low cost. Recently, metal-organic frameworks (MOFs) are appealing materials to build various hybrid nanomaterials through

thermal decomposition under controlled atmospheres.<sup>[48–50]</sup> Different from MOF consisting of metal and organic ligands which are always fabricated via complicated procedures, PB and PBA possess open-framework structure but are much cheaper and easily prepared through simple raw chemicals. Thanks to the altering transition metals, cyano group and a three-dimensional cubic porous network structure, PB and PBA are promising precursors to synthesize various transition metal–carbon based hybrid electrocatalysts. Beyond that, they can obtain different morphology and architecture by adding various surfactant, making them appealing templates to diverse transition metal-based materials.

### 3.1. Unifunctional ORR Electrocatalysts

The study of PB on ORR can be tracked into 1984 when Itaya firstly found its promising ORR activity in acidic aqueous solutions.<sup>[51]</sup> He reported that the reduced form of PB had a catalytic activity to reduce molecular oxygen into water by the four-electron-transfer reaction. However, the activity is still limited due to the inherent low conductivity of PB. To improve the conductivity, Yang's group synthesized a PB/graphene nanocomposite-modified glassy carbon electrode (PB/GE-GCE) through a spontaneous redox reaction, and the PB/GE-GCE exhibited good ORR activity and long-term stability.<sup>[52]</sup> Shanmugam et al. also presented a simple approach to grow PB nanocubes dispersed on carbon composite (PBC/C) for ORR in alkaline medium to improve the conductivity. Although great progress has been made, all the resulted samples show far inferior activity to the commercial Pt/C for ORR with low selectivity.<sup>[53]</sup>

Among all alternatives to Pt-based materials, extensive attention has been paid to Fe, N-based carbon catalysts owing to the low cost and their high catalytic activity induced by Fe-coordinated nitrogen species and nitrogen incorporation. PB assembled by iron components with N-containing ligands thus draws wide attention as a hopeful precursor or template to fabricate Fe, N-based carbon catalysts. However, different from other iron-based MOFs which prefers to form Fe–N–C moiety after carbonization, the product of PB after pyrolysis is mainly iron carbide  $\text{Fe}_3\text{C}$  due to the high content of iron in PB.<sup>[54]</sup> Compared to other methods to prepare  $\text{Fe}_3\text{C}$  with tedious procedures and raw chemicals,<sup>[54–56]</sup> the  $\text{Fe}_3\text{C}$  can be easily obtained from single precursor PB with only high temperature pyrolysis, and the resulted  $\text{Fe}_3\text{C}$  nanoparticles are much uniform and encapsulated by N-doped carbon owing to the unique composition and structure of PB. As a result of the core-shell structure, the  $\text{Fe}_3\text{C}$  in carbon materials always show promising activity for electrocatalysis resulting from the electronic interaction between the confined metal nanoparticles and carbon shells.<sup>[57]</sup>

Except using PB as a single precursor, the hybrids derived from PB together with other conductive substrates are also widely pursued. A nitrogen-doped core-shell-structured porous  $\text{Fe}/\text{Fe}_3\text{C}@\text{C}$  nanoboxes supported on reduced graphene oxide (RGO) sheets (N-doped  $\text{Fe}/\text{Fe}_3\text{C}@\text{C}/\text{RGO}$ ) was reported by

Chen's group via using graphene oxide (GO) and PB nanocubes as precursors, as shown in Figure 3.<sup>[58]</sup> The PB nanocubes here not only act as precursor, but also a self-sacrificing template for the formation of porous nanoboxes. Thanks to the rich –CN group in PB, the nitrogen-containing species formed during pyrolysis in Ar benefited to the reduction of GO and nitrogen dopant in carbon shells and GO simultaneously. Compared to the N-doped  $\text{Fe}/\text{Fe}_3\text{C}@\text{C}$  without N-doped RGO (NRGO) (Figure 3c–e), the N-doped  $\text{Fe}/\text{Fe}_3\text{C}@\text{C}/\text{RGO}$  offers more active sites from both nitrogen-doped  $\text{Fe}/\text{Fe}_3\text{C}@\text{C}$  and NRGO sheets. Besides, the NRGO in the N-doped  $\text{Fe}/\text{Fe}_3\text{C}@\text{C}/\text{RGO}$  (Figure 3f–h) also acts as a bridge to connect the neighbouring nanoboxes and enhances the overall electrical conductivity, which facilitates the charge transport through the carbon shells/RGO sheets and improves the stability of the hybrid. As a result, the hybrid N-doped  $\text{Fe}/\text{Fe}_3\text{C}@\text{C}/\text{RGO}$  exhibits much better electrocatalytic activity with a much more positive ORR onset potential of 1 V and a higher half-wave potential of 0.93 V than N-doped  $\text{Fe}/\text{Fe}_3\text{C}@\text{C}$  in alkaline condition. What's more, the hybrid exhibits exceptional methanol tolerance and outstanding durability compared with the commercial Pt/C catalyst as well. Subsequently, Cui et al. also successfully prepared 3D  $\text{Fe}/\text{Fe}_3\text{C}$  N-doped graphene aerogel ( $\text{Fe}/\text{Fe}_3\text{C}@\text{N-rGO}$  aerogel) with a hierarchical pore system for ORR.<sup>[59]</sup> As displayed in Figure 3i, particle agglomeration during the pyrolysis can be effectively hampered by directly anchoring PB nanoparticles on GO, affording a catalyst with numerous highly active centres and greatly enhancing active site accessibility. It is proposed that the excellent ORR activity of  $\text{Fe}/\text{Fe}_3\text{C}@\text{N-rGO}$  catalyst is attributed to its synergistic effects between  $\text{Fe}_3\text{C}$  and graphitic carbon besides rich accessible active sites. Although it is not in direct contact with the electrolyte,  $\text{Fe}_3\text{C}$  can activate the surrounding graphitic carbon layers towards ORR, and the protecting carbon shells protected the  $\text{Fe}_3\text{C}$  cores from dissolution and promoted charge transfer in turn.

Despite high activity of PB-derived materials, the selectivity and the performance especially in acidic electrolyte of those hybrids need to be further improved. By substituting the ferrous site or ferric site in PB with cobalt, the PBAs containing iron, cobalt and cyano group have also been intensively investigated. Bimetallic materials integrating the merits of each metal always show better performance than their individuals. Wang et al. demonstrated a composite composed of PBA-CoFe ( $\text{Co}_3[\text{Fe}(\text{CN})_6]_2$ ) and polyaniline (PANI) leading to a highly active M–N–C catalyst after pyrolysis and acid leaching for ORR.<sup>[60]</sup> PANI is widely studied as a good precursor to obtain nitrogen-doping carbon material with good electronic conductivity after pyrolysis. As the polymerization process of PANI can be conducted in aqueous solution and PBA tends to form stable colloidal suspension, PBA with proper ratio can be homogeneously dispersed on PANI during mixture which will greatly promote the processability with final active phase. Through their controlling experiments by adjusting the ratio of PANI and PBA, only 2PANI/PBA composite displays uniform PB nanocrystals growing on PANI (Figure 4a). After pyrolysis, the catalyst 2PANI/PBA composed of FeCo alloy, cobalt nitride and graphite phases (named as C-2PANI/PBA), exhibits superior ORR activity

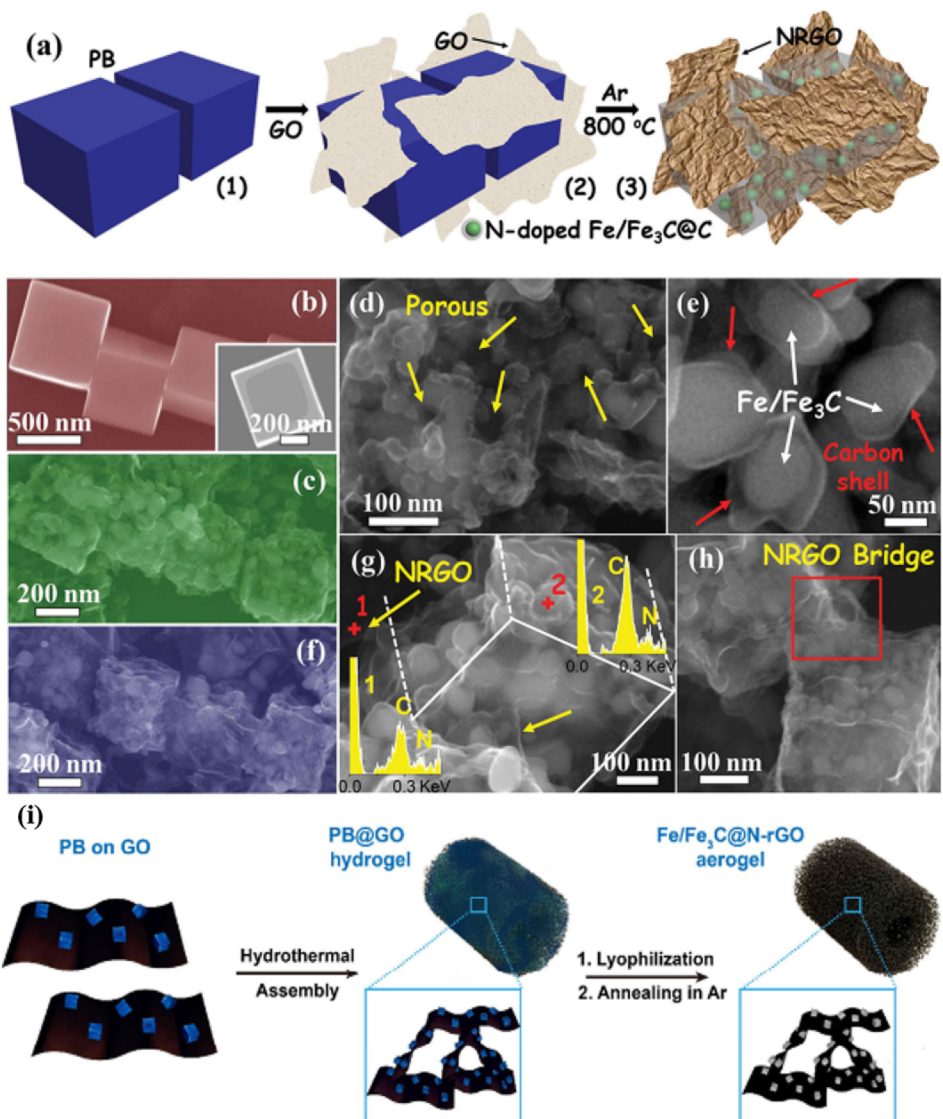


**Figure 3.** (a) Schematic illustration for the synthesis process of N-doped Fe/Fe<sub>3</sub>C@C/RGO. FESEM images of (b) PB, (c–e) N-doped Fe/Fe<sub>3</sub>C@C, and (f–h) N-doped Fe/Fe<sub>3</sub>C@C/RGO. Inset: the corresponding EDX spectra of N-doped Fe/Fe<sub>3</sub>C@C/RGO.<sup>[58]</sup> Reprinted (adapted) with permission from ref. 58. Copyright (2014) Wiley-VCH. (i) Fabrication process of the 3D Fe/Fe<sub>3</sub>C@N-rGO aerogel catalyst.<sup>[59]</sup> Reprinted (adapted) with permission from ref. 59. Copyright (2017) Springer.

in both alkaline and acidic electrolyte (Figure 4b). Although the performance is slightly inferior to Pt/C, the electron transfer number of C-2PANI/PBA is 3.75–3.98 and 3.70–3.84 in alkaline and acidic electrolyte, respectively, which indicates the resulted catalyst is a four-electron dominant process and has high selectivity compared to other reported PB-based works (Figure 4c–4f). Except N-doping in carbon materials, other heteroatoms doping, such as P and S, is also an effective way to improve the activity of catalyst by providing additional active sites. Recently, Zhao et al. have reported an iron-cobalt alloy nanoparticle encapsulated in peapod-like carbon nanotubes which are co-doped by sulphur and nitrogen.<sup>[61]</sup> The resulted catalyst FeCo@N,S-CNTs was facilely prepared via pyrolyzing PBA-FeCo ( $\text{Fe}_3[\text{Co}(\text{CN})_6]_2$ ) and trithiocyanuric acid (TCA) in an argon atmosphere. Electrochemical results show that sulphur co-doping with nitrogen can dramatically boost the catalytic

activity to ORR in contrast to that of FeCo alloy encased in carbon nanotubes with only N-dopant, highlighting the significance of doping and structuring deliberately in the development of more efficient catalysts based on metal nanoparticles grown in CNTs for high-performance electrochemical energy devices.

### 3.2. Unifunctional OER Electrocatalysts

Since OER reaction happens at different potential range from ORR, the requirements for OER catalysts are different, and they should be stable and resistant to corrosion at high potential range. Usually, the materials for OER are mainly transition metal oxides, sulphides, phosphides and alloys. Due to the tunability and instability of PBA in alkaline condition, they can be

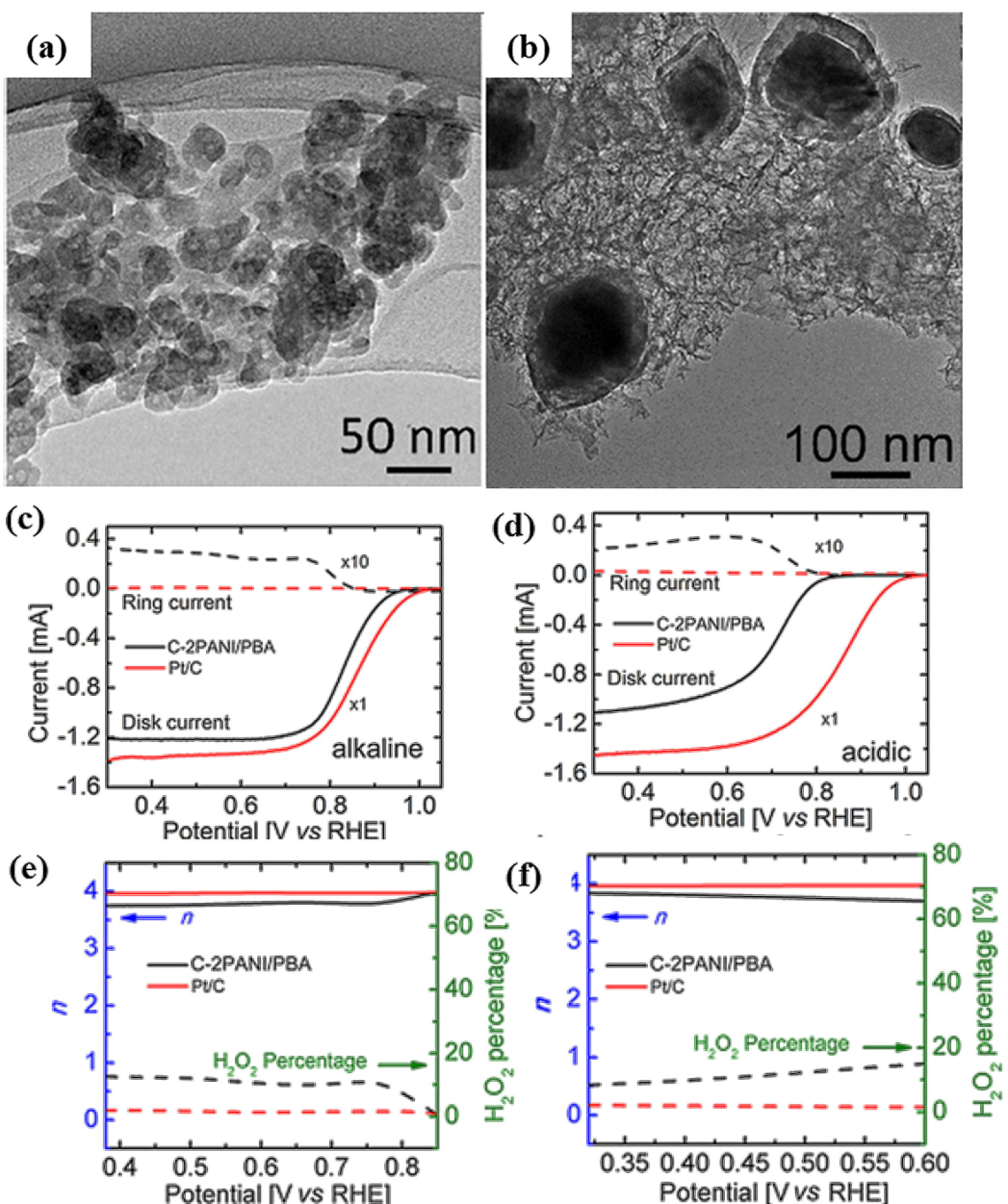


**Figure 4.** (a) SEM image of 2PANI/PBA. (b) TEM image of C-2PANI/PBA. The RRDE voltametric response of C-2PANI/PBA in O<sub>2</sub>-saturated (c) 0.1 M KOH and (d) 0.5 M H<sub>2</sub>SO<sub>4</sub>, respectively, measured at the rotating rate of 1600 rpm with a scan rate of 10 mV s<sup>-1</sup>. A commercial Pt/C catalyst with 20 wt % Pt loading is used as the reference material. The acidic electrolyte is 0.1 M HClO<sub>4</sub> for Pt/C to avoid possible poisoning of Pt by the sulphur species. Summary of H<sub>2</sub>O<sub>2</sub> yield and electron transfer number (e) in alkaline and (f) acidic electrolytes. For all RRDE measurements, the catalysts loading is 0.28 mg cm<sup>-2</sup>.<sup>[60]</sup> Reprinted (adapted) with permission from ref. 60. Copyright (2016) American Chemical Society.

promising templates or precursors to synthesize various active OER materials besides directly carbonization to form core-shell alloy or metal–carbon hybrids.<sup>[62,63]</sup> For instance, Lou's group used cubic PBA-NiCo ( $\text{Ni}_3[\text{Co}(\text{CN})_6]_2 \cdot x\text{H}_2\text{O}$ ) as precursor to synthesize Ni–Co mixed oxide nanocages consisting of pyramid-like walls.<sup>[64]</sup> The cubic PBA-NiCo was first prepared following a modified precipitation method by adding sodium citrate, and it not only acted as a precursor here but also a template to induce the formation of cubic nanocage via a facile anisotropic ammonia etching at room temperature (Figure 5a–f). After calcination in air at 350 °C for 2 h, the as-prepared

Ni–Co cubic nanocages were transformed into the Ni–Co mixed oxides nanocages. According to different morphology after various etching time (Figure 5g), it can be concluded that the etching occurs preferentially at the corners on the PBA Ni–Co cubes and the etching rate is faster along the body diagonal direction of the cubes, which can be originated from the different reactivity between the edge and plane surface of the precursor nanocubes. Finally, the catalyst exhibits a small overpotential of 0.38 V for OER at the current density of 10 mA cm<sup>-2</sup>, and good durability in alkaline medium. The enhanced OER activity of the Ni–Co mixed oxide nanocages

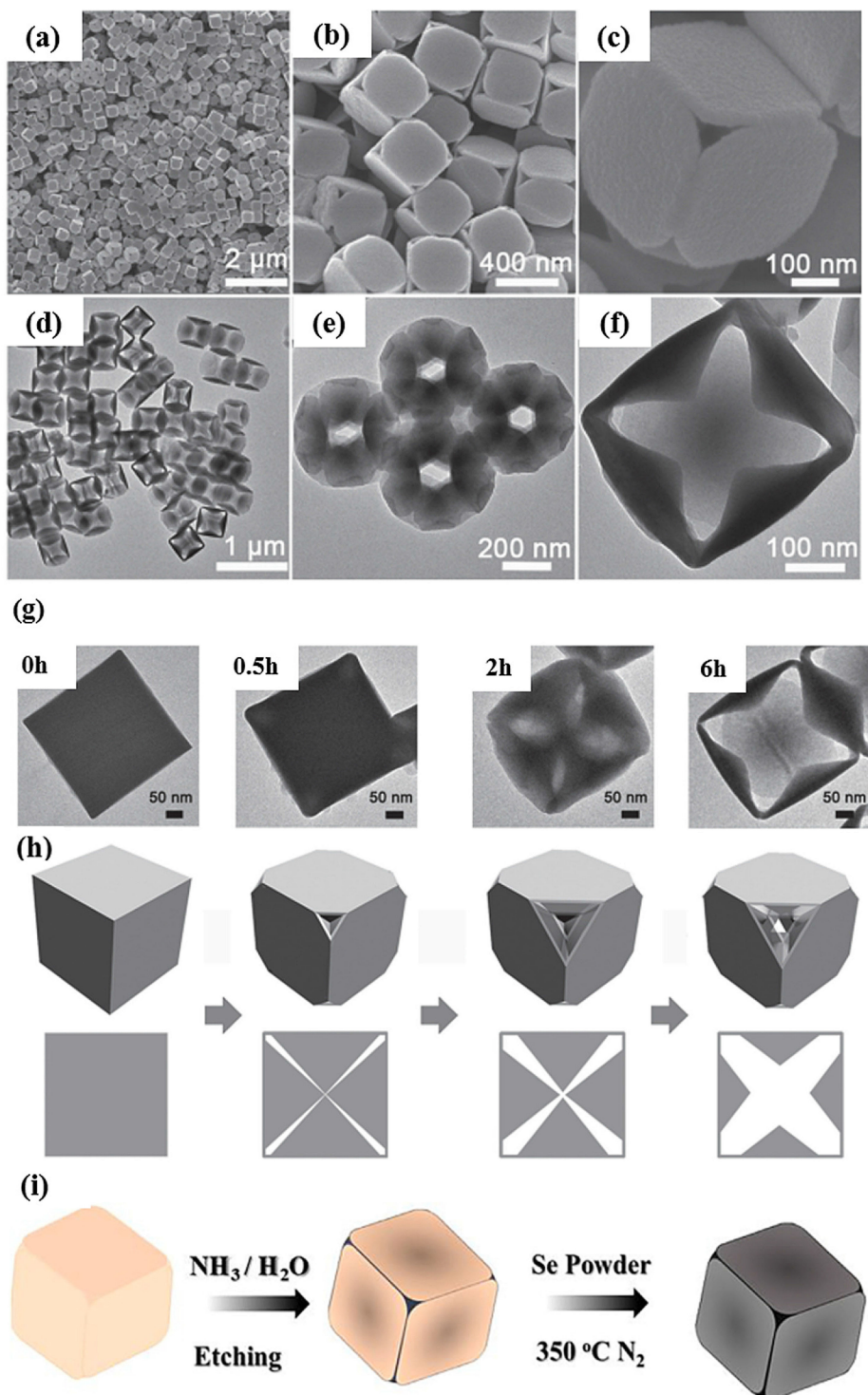


**Figure 5.** (a–c) FESEM and (d–f) TEM images of the PBA Ni–Co cages with an average size of 400 nm. (g) TEM images of the etching products obtained after reacting 20 mg of PBA Ni–Co cubes with 2.5 mL of ammonia at room temperature for 0 h, 0.5 h, 2 h, and 6 h. (h) The corresponding schematics illustrate the formation process of the PBA Ni–Co cages.<sup>[64]</sup> Reprinted (adapted) with permission from ref. 64. Copyright (2016) Wiley-VCH. (i) Schematic illustration of as-synthesized CoSe<sub>2</sub> nanoboxes.<sup>[66]</sup> Reprinted (adapted) with permission from ref. 66. Copyright (2018) Elsevier.

can be accredited to their complex hollow porous 3D cage-like structure and the high surface-area-to-volume ratio of the open structure providing a large electrode-electrolyte contact area. Thereafter, Paik et al. also reported a Co<sub>3</sub>O<sub>4</sub> microframes for OER from PBA-CoCo (Co<sub>3</sub>[Co(CN)<sub>6</sub>]<sub>2</sub>) microcubes via ammonia etch-

ing and annealing in air.<sup>[65]</sup> Kim et al. also presented a CoSe<sub>2</sub> nanoboxes for efficient OER by the reaction of PBA-CoCo nanocubes with ammonia and following calcination with selenium powder,<sup>[66]</sup> as the schematic in Figure 5h. Except etching by ammonia, PBA can be converted into different

components with hollow structure by anion exchange under base condition, such as sulphides and oxides,<sup>[67–70]</sup> thus, many works can be developed from PB or PBA to produce aimed transition metal-based materials for electrocatalysis.

Among all transition metal-based materials, transition metal phosphides (TMPs) have been extensively pursued as promising candidates for OER due to their high activity, high stability, and high conductivity. It has been firstly reported by Hu's group that Ni<sub>2</sub>P even shows better OER performance than nickel oxides and nickel hydroxides.<sup>[71]</sup> However, it is hard to accurately estimate the inherent activity of different nickel-based electrocatalysts as they are usually prepared using different precursors and templates with different morphologies. Inspired by this fact, Paik's group used PBA-NiNi

(Ni(H<sub>2</sub>O)<sub>2</sub>[Ni(CN)<sub>4</sub>]) with well-defined structure as an ideal template and precursor to prepare nickel phosphides, nickel hydroxides and nickel oxides with similar porous plate-like nanostructures.<sup>[72]</sup> As shown in schematic in Figure 6a, Ni(OH)<sub>2</sub> porous nanoplates were obtained by the ion exchange reaction between the PBA-NiNi and NaOH solution, which can be described below:  $\text{Ni}(\text{H}_2\text{O})_2[\text{Ni}(\text{CN})_4](\text{s}) + 2\text{OH}^-(\text{aq}) \rightarrow \text{Ni}(\text{OH})_2(\text{s}) + \text{Ni}(\text{CN})_4^{2-}(\text{aq})$ .<sup>[71]</sup> The nanoporous NiO nanoplates were prepared by annealing PBA-NiNi in an air atmosphere. While the Ni-P porous nanoplates were obtained through low-temperature phosphidation of PBA-NiNi under an argon atmosphere. The FESEM, TEM images and EDX mapping of the single Ni-P nanoplate confirm its rough and porous feature (Figure 6b). Furthermore, the HRTEM image proves that Ni-P species are

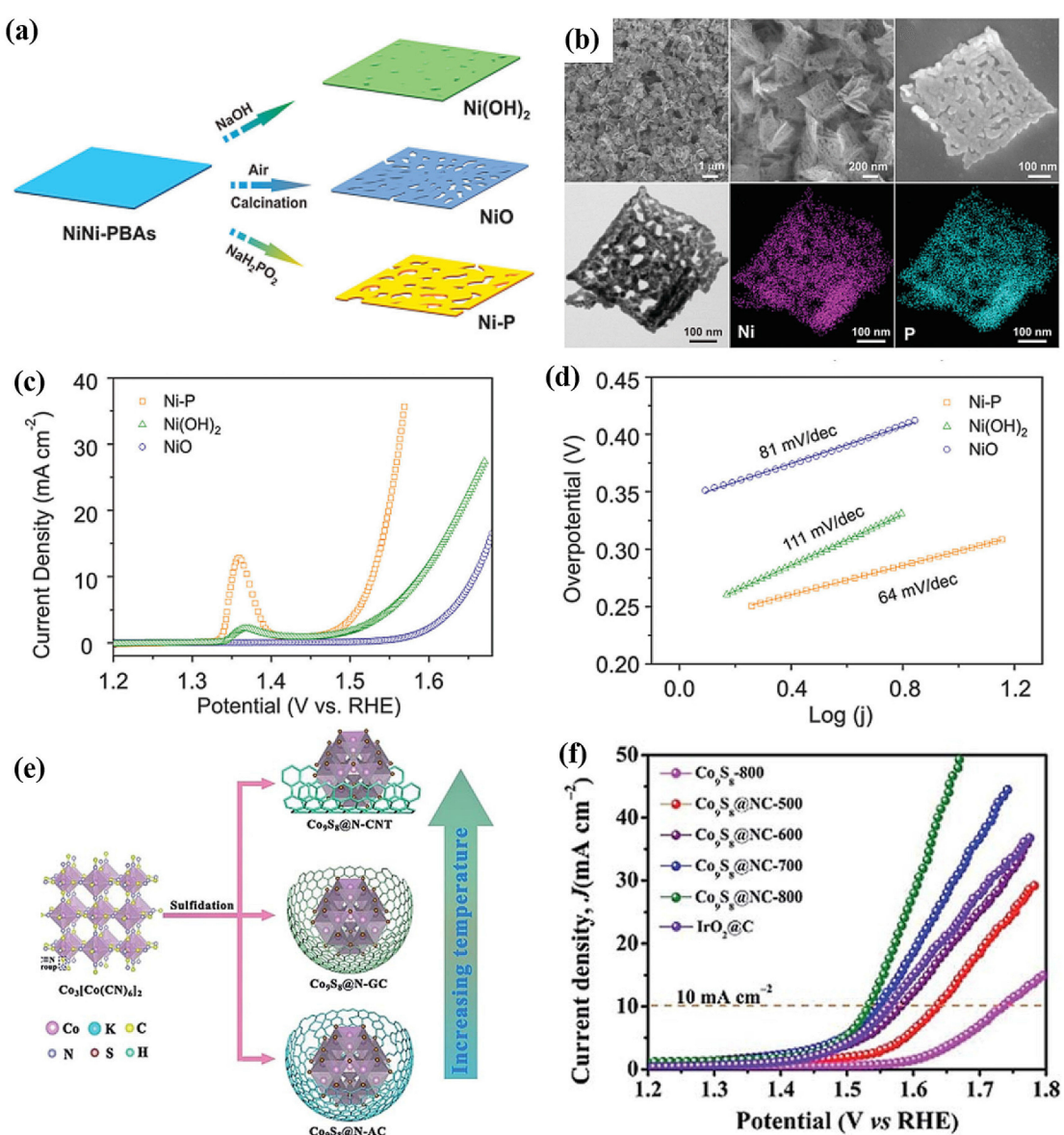


**Figure 6.** (a) Scheme for the formation of Ni(OH)<sub>2</sub>, NiO, and Ni-P porous nanoplates from PBA-NiNi. (b) FESEM images of Ni-P porous nanoplates, TEM image and elemental mapping of a single Ni-P nanoplate. (c) LSV curves and (d) Tafel plots of Ni-P, Ni(OH)<sub>2</sub> and NiO porous nanoplates in 1.0 M KOH.<sup>[72]</sup> Reprinted (adapted) with permission from ref. 72. Copyright (2016) The Royal Society of Chemistry. (e) Synthetic procedure for the preparation of Co<sub>9</sub>S<sub>8</sub>@NC hybrid composites. (f) LSV curves of Co<sub>9</sub>S<sub>8</sub>-800, Co<sub>9</sub>S<sub>8</sub>@NC-T (T = 500, 600, 700, and 800).<sup>[73]</sup> Reprinted (adapted) with permission from ref. 73. Copyright (2018) The Royal Society of Chemistry.

shielded by a layer of amorphous carbon with a thickness of around 2–3 nm. Remarkably, Ni–P porous nanoplates with mixed phases of  $\text{Ni}_5\text{P}_4$  and  $\text{Ni}_2\text{P}$  exhibit a better OER activity in comparison to  $\text{Ni}(\text{OH})_2$  and  $\text{NiO}$  porous nanoplates (Figure 6c–6d). According to XPS results, the nickel phosphides were partially oxidized to nickel oxides/hydroxides on the surface during the OER process. Related to other reported works, the *in situ* generated oxidized nickel species were then regarded as primary active sites for OER. In summary, the superior electrocatalytic activity of Ni–P nanoplate can be ascribed to the porous nanostructure, the incorporation of amorphous carbon from PBA and the *in situ* generated oxidized nickel species during OER, all of which can maximize the number of exposed active sites, facilitate the diffusion of reactants in the electrolyte, and improve the charge transfer capability. This work highlights the importance of phosphides in OER and the benefits of PBA precursor to various OER catalysts. Except monometallic phosphide, thereafter, Lu's group reported a bimetallic phosphide with hollow structure composed of well-dispersed  $\text{Ni}_5\text{P}_4/\text{Fe}_3\text{P}$  in N doped carbon derived from phosphidation of PBA-NiFe ( $\text{Ni}_3[\text{Fe}(\text{CN})_6]_2 \cdot \text{H}_2\text{O}$ ). To avoid collapse of the hollow nanostructure forming severely aggregated nanoparticles, they introduced an inert protection layer  $\text{SiO}_2$  coating on PBA-NiFe before undergoing high temperature phosphorization. After etching by HF, the resulted electrocatalyst N-doped C/ $\text{Ni}_5\text{P}_4/\text{Fe}_3\text{P}$  maintained the hollow nanocubes structure and achieved excellent electrocatalytic efficiencies ( $\eta_{10}=252$  mV and  $\eta_{250}=385$  mV) and eminent long-term stability by drop-casting on a graphite electrode. Likewise,  $\text{Co}_9\text{S}_8$  with N-doped carbon matrixes were also obtained from PBA-CoCo by a simple sulphuration and carbonization step under mixture gas of  $\text{H}_2$  and Ar, which was described by Fang's group.<sup>[73]</sup> This experiment demonstrates the temperature plays an important role to the carbon morphology and the electronic coupling effect between carbon and  $\text{Co}_9\text{S}_8$ . Density functional theory (DFT) calculations indicated that the  $\text{Co}_9\text{S}_8@\text{N-CNT}$  composites (sulphured at 800 °C) had faster electron transfer ability as well as optimal adsorption free energy of oxygen, which both lead to the improved OER catalytic activity (Figure 6f). Herein, PBAs are promising materials to fabricate TMP or TMS with carbon hybrid materials owing to the flexible morphology which can act as the sacrificial template and the rich –CN group which can be carbon or nitrogen source. However, it is still important to deliberately control the annealing temperature to obtain effective phase and prevent aggregation. Besides, choosing proper PBAs and shaping them into optimal architecture to expose more effective active sites are also vital to determine the final performance of resulted electrocatalysts.

Except being used as templates or precursors, the study of PBAs directly applied on oxygen evolution started at 2013 when Galan-Mascaros et al. firstly reported molecule-based material cobalt hexacyanoferrate (CoHCF) exhibiting outstanding long-term stability at ambient conditions and neutral pH for weeks, which is even competitive with state-of-the-art metal oxides.<sup>[74]</sup> Following that, CoHCF thin films formed by chemical etching of metal hydroxide carbonate (Co–HC) template on FTO with  $\text{K}_3\text{Fe}(\text{CN})_6$  was reported by the same group. The

CoHCF in their work can promote OER remarkably and possess good stability under wide pH range ( $1 < \text{pH} < 13$ ).<sup>[75]</sup> This work offers a method to use CoOx template for the CoFe nuclei growth avoiding crystallite agglomeration and a densely packed film contrary to the situation when using drop coating or electrodeposition methods. Sequentially, Song et al. also reported a self-supported PBA-CoCo fabricated by using the Co–HC on carbon cloth (CC) as the template. The PBA-CoCo@CC exhibited excellent OER activity in pH=14 with current density of  $10 \text{ mA cm}^{-2}$  at only 240 mV overpotential, which surpasses its analogue fabricated without any template and the state-of-the-art noble metal catalyst  $\text{RuO}_2$ .<sup>[76]</sup> Those works inspire people to pay more attention to original PB and PBA on OER other than their derivations. As we know, PB and PBA with open framework structure are not stable in alkaline medium.<sup>[34,64]</sup> It was found that the structure of PBA-CoCo@CC transferred into the layered hydroxide-oxyhydroxide which can enhance the electron transport and mass transfer during OER process. However, more deep analysis is necessary to comprehensively understand the reason of the transformation and why the derived species are more active than their counterparts. Generally, this template approach provides a facile way to prepare PBA-based electrocatalysts for OER with high current densities and excellent stability for the oxygen evolution owing to easy electron transport, and strong mechanical stability.

### 3.3. Bifunctional Electrocatalysts

For rechargeable metal–air batteries, air electrodes should be capable of catalysing both the ORR and OER efficiently. Compared to use combinations of multiple functional components, employing an effective and economical bifunctional oxygen catalyst is much desirable. Thus, a great deal of research has been made to develop earth-abundant bifunctional electrocatalysts, such as transition metal oxides,<sup>[77]</sup> carbides,<sup>[78]</sup> alloys,<sup>[79]</sup> and transition metal–carbon hybrids.<sup>[80]</sup> PB and PBAs with adjustable framework compositions and pore structures, show great potential as precursors to various active components for ORR and OER. In 2015, Nanda's group reported a bifunctional electrocatalyst by pyrolyzing PB as a single source at 750 °C.<sup>[81]</sup> After washed in concentrated hydrochloric acid solution for overnight, the resulted bamboo-like N-doped graphitic nanotubes encapsulating  $\text{Fe}/\text{Fe}_3\text{C}$  nanoparticles (BGN) transformed to hollow N-doped graphitic (N–HG) nanostructures, both of which show promising activity for ORR and OER. Through further investigation, they observed that the ORR activity is shown to be improved for N–HG ( $E_{\text{onset}} = -0.05$  V vs.  $\text{AgCl}/\text{Ag}$ ) which is even comparable to commercial Pt/C ( $E_{\text{onset}} = -0.03$  V vs.  $\text{AgCl}/\text{Ag}$ ), while the OER performance decreases after removing the  $\text{Fe}_3\text{C}/\text{Fe}$  core from BGN. The results suggest that the excellent ORR and OER catalytic activity are associated with both the encapsulated and hollow graphitic nanostructures. Through quantifying the N content from XPS, the results reveal that 94% of N-doping in N–HG are ascribed to pyridinic and pyrrolic N, which leads to the enhanced performance of  $\text{O}_2$  reduction.<sup>[82]</sup> Furthermore, the percentage of N-doping de-

creases from 8.6 to 4.8% with the increasing temperature from 750 to 850 °C, because carbon nitride decomposes into N<sub>2</sub> gas that does not take part in the doping at high temperatures. Thus, the pyrolysis temperature is significant to affect the N-doping content or species and finally determine the electrochemical performance. Similarly, Chen et al. used PBA-ZnCo (Zn<sub>3</sub>[Co(CN)<sub>6</sub>]<sub>2</sub>) as single precursor to synthesize spherical Co<sub>3</sub>ZnC/Co nanojunctions encapsulated in highly nitrogen doped graphene layers (Co<sub>3</sub>ZnC/Co@CN) by one-step annealing,<sup>[83]</sup> and the schematic is shown in Figure 7a. With the increasing temperatures, the products exhibit different phases from Co<sub>3</sub>ZnC to metallic Co (Figure 7b). Eventually, the catalyst obtained at 650 °C (denoted as S-650) shows the best OER performance in 1 M KOH with a low overpotential of only 366 mV at 10 mA cm<sup>-2</sup> (Figure 7c-7d), and it also has a low

onset potential and cathodic peak potential at 0.912 V and 0.814 V for ORR in 0.1 M KOH. In this study, the authors argue that the prominent electrocatalytic activity of S-650 is mainly attributed to its chemical composition and unique structure of the Co<sub>3</sub>ZnC/Co heterojunction which has the stronger electron coupling effect to facilitate electron transfer from metallic Co to Co<sub>3</sub>ZnC. The formation of electrophilic metallic Co and nucleophilic Co<sub>3</sub>ZnC can promote the nucleophilic reaction/electrophilic reaction by OH<sup>-</sup> with the intermediates to accelerate OER/ORR, respectively. Besides, the N-doped graphene layers provide extra O<sub>2</sub> adsorption sites to enhance electrocatalytic activity and the protection to sustain the stability during the electrocatalytic reaction. Compared to PB, PBA provides a promising way to directly fabricate diverse transition metal-based electrocatalysts with nanojunctions as

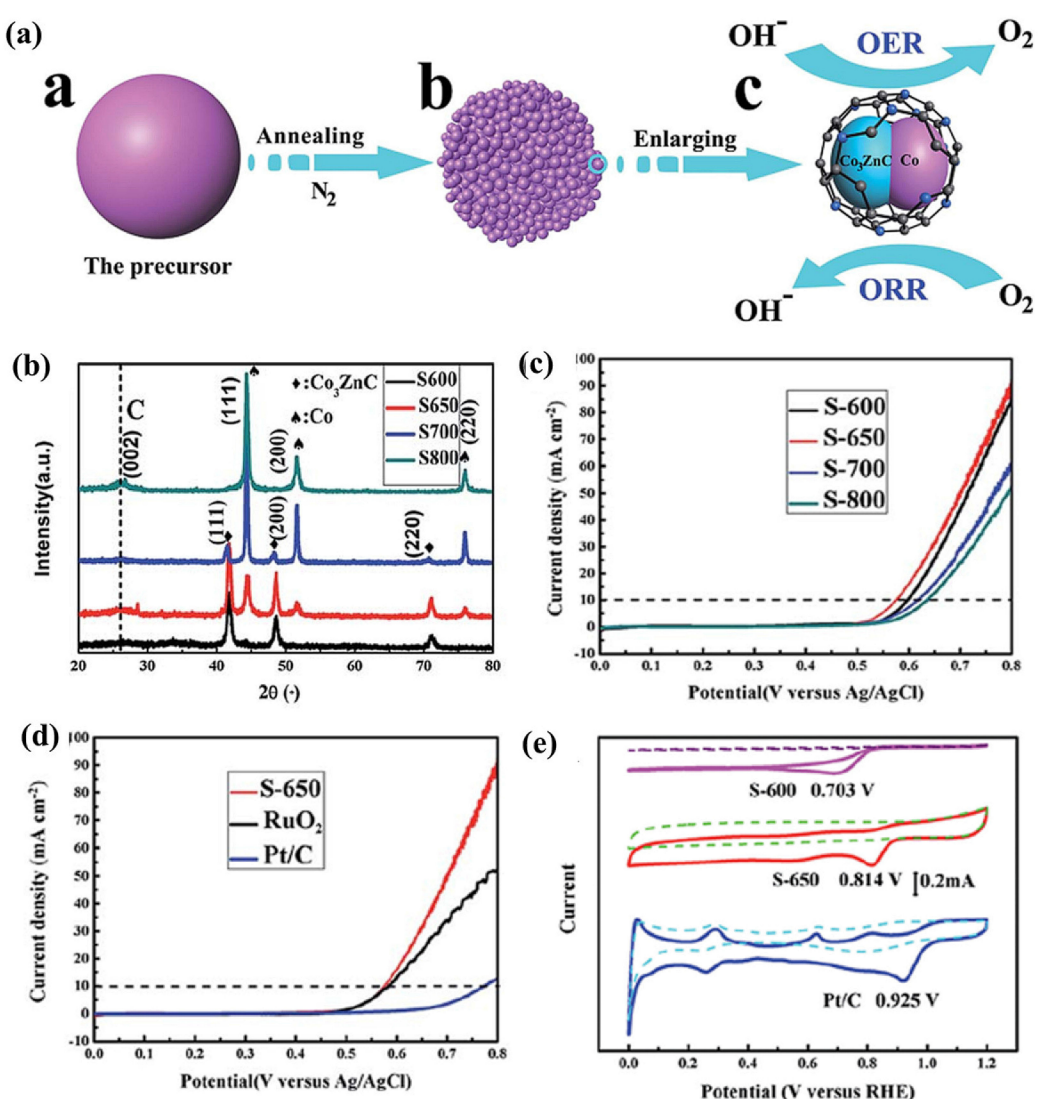


**Figure 7.** (a) The synthetic route and model of the Co<sub>3</sub>ZnC/Co nanojunctions encapsulated in nitrogen-doped graphene layers. (b) The XRD patterns of S-600, S-650, S-700, and S-800. (c) OER polarization curves of samples synthesized at different temperatures with the same mass loading in 1 M KOH solution. (d) OER polarization curves of S-650, RuO<sub>2</sub> and Pt/C with the same mass loading. (e) CV curves of S-600, S-650 and Pt/C in O<sub>2</sub>-saturated (solid line) or N<sub>2</sub>-saturated 0.1 M KOH (dashed line) LSV curves of S-650 at different rotation rates and the corresponding Koutecky-Levich plots at different potentials.<sup>[83]</sup> Reprinted (adapted) with permission from ref. 83. Copyright (2016) The Royal Society of Chemistry.

well. Although the OER performance of S-650 comprised of  $\text{Co}_3\text{ZnC}/\text{Co@CN}$  is superior to commercial  $\text{RuO}_2$  and  $\text{Pt/C}$  catalysts under alkaline conditions, the ORR of this catalyst is still far inferior to  $\text{Pt/C}$ . Thus, further optimization is needed to improve the ORR performance without compromising OER activity. Recently, Chen's group synthesized CoFe nanoalloy particles encapsulated in nitrogen doped carbon and nitrogen-doped carbon nanotubes from PBA-CoFe. As for the bifunctionality for both OER and ORR, an extremely low potential difference of  $\sim 0.87$  V between OER at  $10.0 \text{ mA cm}^{-2}$  and ORR at  $3.0 \text{ mA cm}^{-2}$  is achieved, superior to either commercial  $\text{RuO}_2$  or  $\text{Pt/C}$ .<sup>[84]</sup> Except carbides, metal–carbon/nitrogen (M–C/N) composites and alloys, mixed oxides derived from PBA were also reported as effective bifunctional electrocatalysts for ORR and OER. For instance, Li and co-authors reported a series of porous spinel  $\text{Mn}_x\text{Fe}_{1.8-x}\text{Co}_{1.2}\text{O}_4$  with nano-dices morphology, similar crystallite size and high specific surface area from ternary PBA for OER and ORR. During their study, they found the enhanced bifunctional activity could be correlated with octahedral-site  $\text{Mn}^{3+}/\text{Mn}^{4+}$  content.<sup>[85]</sup> Through annealing at different atmosphere, the resulted species may vary with the conditions and consist of different phases. Generally, M–C/N composites and alloys have appealed wide attention in comparison with oxides due to their high conductivity.<sup>[86,87]</sup> In summary, PB and PBAs are indeed cost-effective precursor to different bifunctional electrocatalysts via facile methods.

#### 4. PB/PBA Based Materials Applied in Metal-Air Batteries

In metal-air batteries, the air cathode plays the decisive role in improving battery performance. Even though a great amount of materials has been developed as efficient ORR and OER electrocatalysts under three-electrodes system over the past decades, many of them suffer from poor stability and cyclability during discharging and charging process when applied in actual metal-air batteries. Thus, it is still challenging to fit all possible electrocatalysts in harsh reductive-oxidative environments of metal-air batteries in practice. An ideal cathode electrocatalyst in meta-air battery should be anticorrosive and compatible in corresponding electrolytes besides possessing the active compositions and architectures. Summarizing the progress of electrocatalysts in metal-air batteries derived from PB/PBA will deepen our understanding of how to design proper electrocatalysts and provide some guidance for the development of other MOF derived materials.

##### 4.1. Primary Batteries

As we know, the primary battery is designed to be used once, and not recharged with electricity and reused like a rechargeable battery. Hence, the air cathode will govern the overall performance of primary metal-air batteries. In 2016, Li et al. firstly employed Co@NG-acid derived from PBA-CoCo as the air

catalyst for primary Zn-air batteries.<sup>[88]</sup> As shown in Figure 8a, the metallic cobalt nanoparticles covered by multilayered graphene shells with enriched nitrogen dopant (Co@NG) was prepared by simply annealing PBA-CoCo at  $600^\circ\text{C}$  in Ar. Through leaching out metallic cobalt cores by HCl treatment, the hollow graphene spheres Co@NG-acid was obtained. Both Co@NG-acid and Co@NG exhibit promising activities for ORR in 1 M KOH (Figure 8b). The better performance of Co@NG-acid than that of Co@NG suggests that Co-N–C moieties can be the real active sites for ORR. After employing as the air cathode by uniformly dispersing Co@NG-acid on a hydrophobic carbon fibre paper, the customized primary zin-air filled with 6 M KOH electrolyte presented an open circuit voltage of  $\approx 1.4$  V. Remarkably, it can deliver large current densities of  $55 \text{ mA cm}^{-2}$  and  $255 \text{ mA cm}^{-2}$  at a voltage of 1.20 and 1.0 V, respectively, and also reaches a maximum power density of  $350 \text{ mW cm}^{-2}$  (Figure 8c). Even though they are still inferior to those of battery using Pt/C as the air catalyst, the current density and power density are remarkably enhanced over earlier primary batteries.<sup>[89,90]</sup> Besides, this primary Zn-air battery possesses good durability when galvanostatically discharged at a current density of  $10 \text{ mA cm}^{-2}$  for 14 h and  $50 \text{ mA cm}^{-2}$  for 4.5 h (Figure 8d). Such exceptional performances of the primary Zn-air battery and easy preparation highlight the potential of PB/PBA-derived materials as appealing air catalysts to primary Zn-air batteries. Following that, Cui's group reported a  $\text{Mn}_{x}\text{Co}_{3-x}\text{O}_4/\text{N-Ketjenblack}$  hybrid composing of porous spinel oxides and N-doped carbon materials derived from PBA-MnCo ( $\text{Mn}_3[\text{Co}(\text{CN})_6]_2 \cdot \text{nH}_2\text{O}$ ) for the primary Zn-air battery.<sup>[91]</sup> Different from other works requiring high temperature annealing and inert atmosphere, the composite in their work can be facilely prepared by thermally decomposing PBA-MnCo and gelatine-coated Ketjenblack carbon at  $400^\circ\text{C}$  in air, as the schematic in Figure 8e. Compared to physical mixture of bare  $\text{Mn}_{x}\text{Co}_{3-x}\text{O}_4$  and Ketjenblack,  $\text{Mn}_{x}\text{Co}_{3-x}\text{O}_4/\text{N-Ketjenblack}$  hybrid presents excellent activity due to rich N-species from the gelatine pyrolysis and porous spinel oxide from PBA oxidation, which provides ample active pyridinic N/pyrrolic N for ORR and hydrophobic surface beneficial to oxygen diffusion. Thanks to the efficient mass transfer and moderate interaction, the active sites in the composite can be easily accessed by oxygen, enhancing the performance of ORR kinetics. Figure 8f depicts the polarization curve of different air cathodes in full Zn-air batteries. Obviously,  $\text{Mn}_{x}\text{Co}_{3-x}\text{O}_4/\text{N-Ketjenblack}$  has a lower voltage drop rate than that of the cell catalysed by Pt/C, and the power density of it is 16% higher than that of the Pt/C-catalysed cell at 0.8 V. In addition, the  $\text{Mn}_{x}\text{Co}_{3-x}\text{O}_4/\text{N-Ketjenblack}$  in full cell exhibits excellent rate capability and a fast-dynamic response (Figure 8g). This work inspires us that it is crucial to design electrocatalysts in metal-air batteries with optimal architecture and hydrophobicity for better gas-phase oxygen transfer. Moreover, controlling N-doped species in carbon matrix besides the metal cores is important as well to achieve good performance of metal-air batteries. Pan et al reported an  $\text{Fe}_3\text{C}(\text{Fe})@\text{NDGL}$  consisting of Fe-cluster and  $\text{Fe}_3\text{C}$  nanoparticles (designated as  $\text{Fe}_3\text{C}(\text{Fe})$ ) encapsulated in nitrogen-doped graphitic layers (NDGL) as a new hybrid nanostructure for primary Zn-

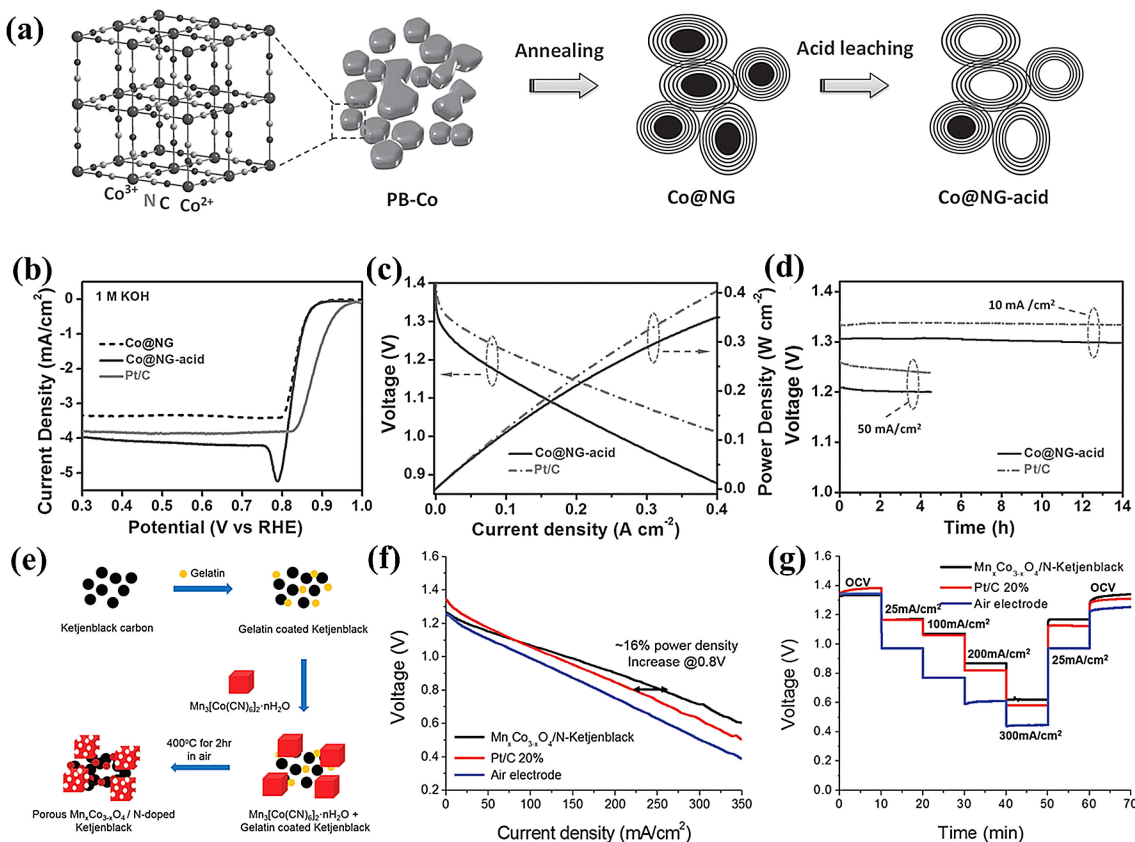


**Figure 8.** (a) Schematic illustration of the synthesis of Co@NG and Co@NG-acid from the cobalt-containing PB-CoCo as the single precursor. (b) Co@NG and Co@NG-acid in  $O_2$  saturated 1 M KOH. All these data were collected at the electrode rotation rate of 1600 rpm. The 20 wt% Pt/C benchmark was also included for comparison. (c) Discharge polarization curve and corresponding power density of Zn-air batteries using Co@NG-acid and Pt/C as the air catalyst. (d) Long-time galvanostatic discharge curves of Zn-air batteries using Co@NG-acid and Pt/C as the air catalyst at 10 mA cm<sup>-2</sup> and 50 mA cm<sup>-2</sup>. The catalyst loading in this study is 1 mg cm<sup>-2</sup> on carbon fiber paper.<sup>[88]</sup> Reprinted (adapted) with permission from ref. 88. Copyright (2016) Wiley-VCH. (e) Schematic illustration of the synthesis of the electrocatalysts derived from Ketjenblack, gelatin, and Mn<sub>3</sub>[Co(CN)<sub>6</sub>]<sub>2</sub>·nH<sub>2</sub>O. (f) Current density-voltage (J–V) profiles of the Pt/C and porous Mn<sub>3</sub>Co<sub>3-x</sub>O<sub>4</sub>/N-Ketjenblack catalysed air electrodes and that of a bare air electrode in Zn-air batteries. (g) Discharge profiles of the Zn-air batteries from low current densities to high current densities (open-circuit voltage (OCV), 25, 100, 200, and 300 mA cm<sup>-2</sup>, and recovery to OCV).<sup>[91]</sup> Reprinted (adapted) with permission from ref. 91. Copyright (2016) Wiley-VCH.

air battery through directly pyrolyzing a mixture of glucose and PB.<sup>[92]</sup> Combining with the DFT calculation, the experimental results prove that the high activity of the catalyst can be attributed to the synergistic effect of an suitable level of nitrogen doping and electrons transfer from Fe<sub>3</sub>C(Fe) to nitrogen-doped graphitic carbon shells. They discovered the whole surface of the NDGL in contact with the electrolyte solution can efficiently capture O<sub>2</sub> molecules, leading to a quick diffusion of reactant to the active sites on the continuous graphene surface. Compared to Pt/C catalyst which can only adsorb O<sub>2</sub> molecules in scattered clusters, the optimized Fe<sub>3</sub>C(Fe)@NDGL catalyst definitely has a larger effectively active surface area, resulting in higher current density and power density. Finally, the full Zn-air battery based on Fe<sub>3</sub>C(Fe)@NDGL air cathode shows a maximum power density of 186 mW cm<sup>-2</sup>, exceeding that with Pt/C catalyst (167 mW cm<sup>-2</sup>). In a word, PB/PBAs as cheap precursors which do not require any organic solvent, template, and other rigid conditions to be synthesized, are very appropriate for production and application in metal-air batteries on large scale.

## 4.2. Rechargeable Batteries

For rechargeable metal-air batteries, the fundamental electrochemistry within cathodic reaction is still under investigation owing to the complicated processes varying with different electrolytes. Thanks to the structural flexibility and compositional tunability, PB/PBA as promising precursors have been applied in different rechargeable metal-air batteries.

### 4.2.1. Aqueous Zn-air Batteries

Rechargeable Zn-air batteries, as the hottest represent in aqueous metal-air batteries, has been intensively investigated. In 2016, Wen et al used PBA-FeCo fabricating a core-shell FeCo alloy coated with N-doped carbon (FeCo@NC) and firstly applied it in rechargeable Zn-air batteries.<sup>[93]</sup> By carbonization of PBA-FeCo in Ar atmosphere at different temperatures, they found FeCo@NC-750 possessing the best bifunctional activity and battery performance of specific capacity of 763 mAh g<sup>-1</sup> due to the synergistic effect between N-doped carbon and

alloy.<sup>[93]</sup> In comparison with other tedious synthesis methods, the alloy@NC derived from PBA, which usually owns controllable stoichiometric ratio, uniform elemental distribution and surface composition, is easily prepared. Except to attain core-shell structured alloy/carbon hybrid by pyrolysis in inert environment, PBA is also of great potential to diverse bimetallic oxides which intrinsically combine the merits of their single-element counterpart with high activity and stability.<sup>[94,95]</sup> It is said the crystallinity and composition of the bimetallic oxides have strong impacts on their electrochemical performance.<sup>[46,96]</sup> To precisely control them, Chen's group demonstrated a general three-stage synthesis strategy to prepare a family of hybrid materials consisting of amorphous bimetallic oxide nanoparticles anchored on N-doped reduced graphene oxide from PBAs.<sup>[97]</sup> Taking the  $\text{Fe}_a\text{Co}_{1-a}\text{O}_x/\text{NrGO}$  ( $a=0\sim 1$ ) as an

example, as shown in Figure 9a, the GO nanosheets were firstly deposited with a positively charged PEI polymer ( $(\text{C}_2\text{H}_5\text{N})_n$ ) layer which can serve as a N-doping source for GO and facilitate the uniform distribution of  $\text{Fe}(\text{CN})_6^{3-}$  anions on negatively charged GO. Next,  $\text{K}_3\text{Fe}(\text{CN})_6$  were added into to the PEI/GO hybrid to form a monolayer of PBA nanocrystals on the surface. Afterward, the  $\text{CoCl}_2$  solution was added drop-wise under vigorous stirring to avoid the formation of large PB/PBA particles. Finally,  $\text{Fe}_a\text{Co}_{1-a}\text{O}_x/\text{NrGO}$  can be obtained by decomposing  $\text{FeCo}/\text{PEI}/\text{GO}$  in air. Through controlling experiments to explore suitable ratios and temperatures, they found  $\text{Fe}_{0.5}\text{Co}_{0.5}\text{O}_x/\text{NrGO}-300$  keeps best activity for both OER and ORR. SEM image and EDX mapping show there is no large particles aggregating on the surface of  $\text{Fe}_{0.5}\text{Co}_{0.5}\text{O}_x/\text{NrGO}-300$  (Figure 9b). While TEM image and SAED pattern confirm the amorphous oxide particles with

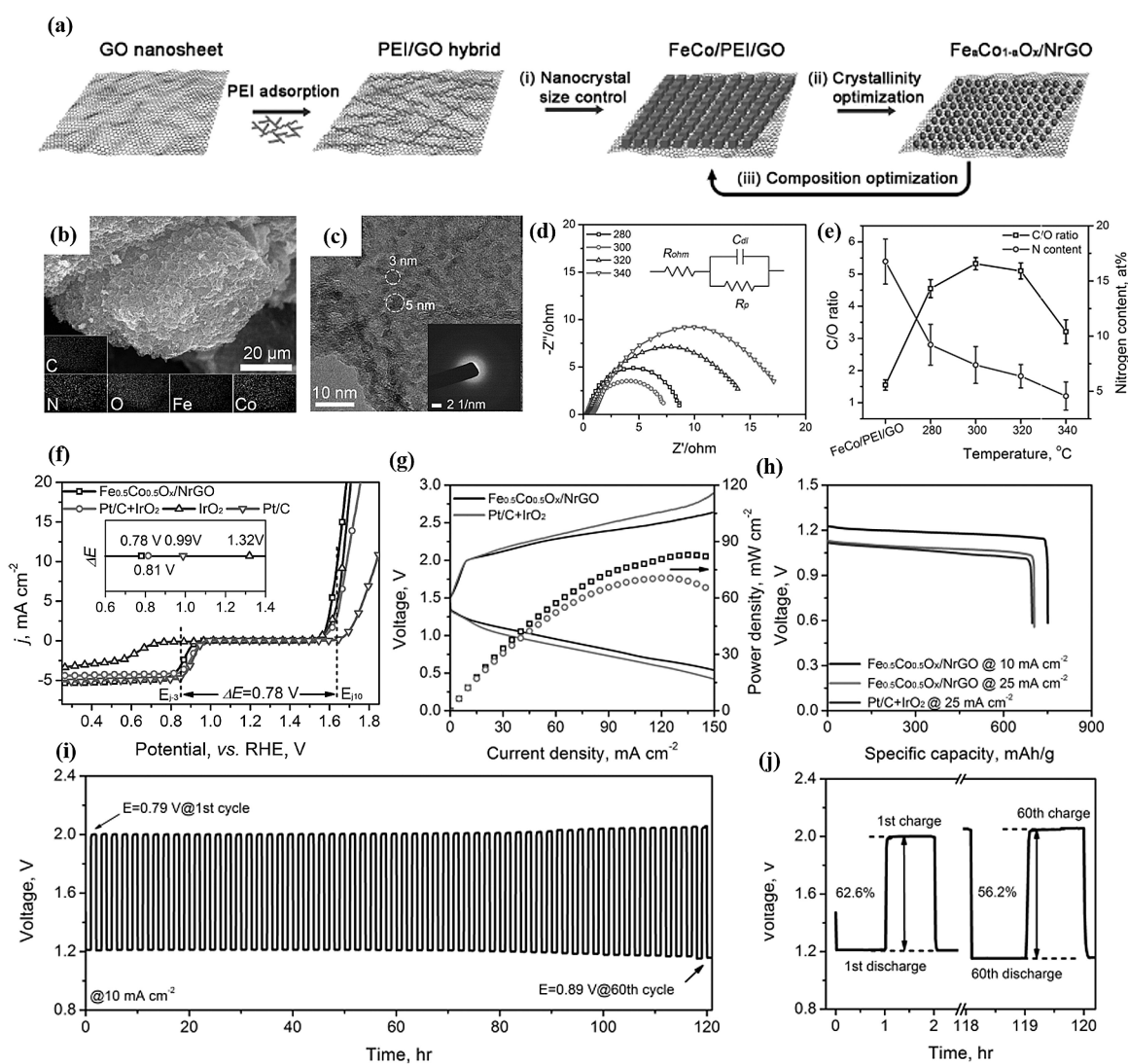


**Figure 9.** (a) Schematic illustration of the synthesis of  $\text{Fe}_a\text{Co}_{1-a}\text{O}_x/\text{NrGO}$  hybrid in a three-stage synthesis approach. (b) SEM image and EDX elemental mappings of  $\text{Fe}_{0.5}\text{Co}_{0.5}/\text{PEI}/\text{GO}$ . (c) TEM images and SAED patterns of  $\text{Fe}_{0.5}\text{Co}_{0.5}\text{O}_x/\text{NrGO}-300$ . (d) Nyquist plots and (e) atomic ratios between  $\text{sp}^2\text{-C}$  and O-bonded C (left) and N contents in  $\text{Fe}_{0.5}\text{Co}_{0.5}\text{O}_x/\text{NrGO}$  hybrids obtained at different temperatures. (f) The overall polarization curves of  $\text{Fe}_{0.5}\text{Co}_{0.5}\text{O}_x/\text{NrGO}$  and commercial  $\text{Pt/C} + \text{IrO}_2$  catalysts for ORR and OER.  $\text{Fe}_{0.5}\text{Co}_{0.5}\text{O}_x/\text{NrGO}$  as a bifunctional air electrode for rechargeable Zn-air batteries in comparison with commercial  $\text{Pt/C} + \text{IrO}_2$  catalysts. (g) Galvanodynamic charge/discharge profiles (left) and power density curves (right). (h) Galvanostatic discharge curves of the primary Zn-air batteries. (i,j) Charge/discharge cycling of a rechargeable Zn-air battery based on  $\text{Fe}_{0.5}\text{Co}_{0.5}\text{O}_x/\text{NrGO}$  at  $10 \text{ mA cm}^{-2}$ .<sup>[97]</sup> Reprinted (adapted) with permission from ref. 97. Copyright (2017) Wiley-VCH.

diameter of 3–6 nm highly dispersing on NrGO surface (Figure 9c). From the Nyquist plot and XPS results (Figure 9d–9e), they reveal that the annealing temperature at 300 °C endows the hybrid  $\text{Fe}_{0.5}\text{Co}_{0.5}\text{O}_x/\text{NrGO-300}$  with optimal electrical conductivity and ionic conductivity. Figure 9f displays the potential difference ( $\Delta E = E_{j10} - E_{j3}$ ) between OER and ORR of  $\text{Fe}_{0.5}\text{Co}_{0.5}\text{O}_x/\text{NrGO-300}$ , which is smaller than that of the Pt/C + IrO<sub>2</sub>, implying its excellent bifunctional activity. The good performance can be credited to the amorphous structure with abundant oxygen vacancies and improved ionic conductivity, proper Fe/Co ratio, strong interactions and synergistic effects between NrGO substrates and  $\text{Fe}_{0.5}\text{Co}_{0.5}\text{O}_x$  nanoparticles. When applied as air electrodes in the practice, the fabricated Zn-air battery full of an electrolyte containing 6 M KOH and 0.2 M ZnCl<sub>2</sub> shows an open circuit potential of 1.43–1.44 V and delivers a peak power density of 86 mW cm<sup>-2</sup> (Figure 9g–9 h). In addition, the battery has a specific capacity of 756 mA h g<sub>Zn</sub><sup>-1</sup> at the discharge current density of 10 mA cm<sup>-2</sup>, which is largely improved compared with the battery using Pt/C + IrO<sub>2</sub>. In addition, it exhibits excellent stability after charging and discharging for 120 h at 10 mA cm<sup>-2</sup> (Figure 9i–9j). Except  $\text{Fe}_{0.5}\text{Co}_{0.5}\text{O}_x/\text{NrGO}$ , other two amorphous bimetallic, like  $\text{Ni}_{0.4}\text{Fe}_{0.6}\text{O}_x$  and  $\text{Ni}_{0.33}\text{Co}_{0.67}\text{O}_x$  are also produced via same procedures for energy conversion. Generally, this work provides an approach to prepare binary, tertiary or even quadruple metal oxides with controllable size, elemental composition, and crystallinity as advanced catalysts for energy conversions applications.<sup>[97]</sup>

#### 4.2.2. Nonaqueous Li–O<sub>2</sub> Batteries

Li–O<sub>2</sub> batteries as a typical nonaqueous meta-air battery have been regarded as the promising alternative to traditional lithium-ion batteries due to their high theoretical energy density. Different from aqueous Zn-air batteries, they suffer from electrolyte instability, poor cycle stability and high overpotential. Additionally, the discharging products at cathode always have low solubility to electrolytes and are easily deposited on air cathode to block the transportation of electrolytes and oxygen. Thus, it is highly desirable to design porous catalysts with well-defined hollow structure and large surface areas to provide sufficient catalytically active sites improving battery performance, regardless of what type of catalysts are developed. PBAs with a controlled open-framework structure hence come to the view as ideal precursors to synthesize porous transition metal-based materials. Specifically, the derivative metal oxides from PBAs usually exhibit the desired morphology, large surface area, uniform pore structure and hierarchical pore size.<sup>[98]</sup> For example, Zhang and co-workers synthesized a hierarchical porous  $\delta\text{-MnO}_2$  nanoboxes derived from PBA-MnCo applying in Li–O<sub>2</sub> batteries.<sup>[99]</sup> As displayed in Figure 10a, the nanosized well-defined cubic PBA-MnCo precursors with smooth facets were fabricated by a self-assembly method in the first step. Then, Mn<sub>3</sub>O<sub>4</sub> nanoboxes were obtained by the ion exchange of PBA-MnCo with NaOH at room temperature. Finally, MnO<sub>2</sub> nanoboxes were obtained by oxidizing the hollow Mn<sub>3</sub>O<sub>4</sub> nanoboxes with (NH<sub>4</sub>)<sub>2</sub>S<sub>2</sub>O<sub>8</sub>. The

TEM images show the transformation from PBA to MnO<sub>2</sub> (Figure 10b–10d). Apparently,  $\delta\text{-MnO}_2$  possesses size range from 150 to 250 nm, and BET results suggest its rich meso-macropores with an extremely large surface area up to 249.3 m<sup>2</sup> g<sup>-1</sup>. Through investigating the correlation of the morphology of Mn<sub>3</sub>O<sub>4</sub> intermediate products with the concentration of NaOH, they found that the concentration of NaOH solution too low ( $\leq 0.001$  M) or too high ( $\geq 0.02$  M) will destroy the hollow nanobox structure. Thus, using alkaline solution with suitable concentration to precisely manipulate the ion exchange rate is significant to control the hollow porous morphology. When the hierarchical porous  $\delta\text{-MnO}_2$  nanobox was employed as cathode catalyst in the Li–O<sub>2</sub> battery with 1 M lithium trifluoromethanesulfonate/tetraethylene glycol dimethyl ether (LiCF<sub>3</sub>SO<sub>3</sub>/TEGDE) as electrolyte, it delivered a high discharge capacity of 4368 mA h g<sup>-1</sup> with smaller overpotentials than that using the commercial Vulcan XC-72 carbon electrode at 0.08 mA cm<sup>-2</sup> (Figure 10e). Besides, the specific capacity was enhanced as well as the capacity retention at various current densities (Figure 10f). At a rate of 0.16 mA cm<sup>-2</sup>, the battery with a hierarchical porous  $\delta\text{-MnO}_2$  nanobox catalyst possesses long cycle stability up to 248 cycles and 112 cycles without obvious capacity deterioration at the limited discharge capacity of 500 mA h g<sup>-1</sup> and 1000 mA h g<sup>-1</sup> (Figure 10i–10j),<sup>[99]</sup> suggesting hollow porous  $\delta\text{-MnO}_2$  nanobox as an excellent cathode catalyst for the Li–O<sub>2</sub> battery. Similarly, Chen's group reported a hierarchical porous Co<sub>3</sub>O<sub>4</sub> nanobox from PBA-CoFe as efficient cathode catalysts for Li–O<sub>2</sub> batteries in the same way.<sup>[100]</sup> The obtained porous Co<sub>3</sub>O<sub>4</sub> nanoboxes with large surface area up to 272.5 m<sup>2</sup> g<sup>-1</sup> presented enhanced capacity, better rate performance and excellent cycle stability in comparison with the EC-300 J carbon cathode. In summary, PBAs indeed provide a facile fabrication approach to develop advanced oxide catalysts with controllable morphology for Li–O<sub>2</sub> batteries compared to hydrothermal and calcination methods which usually result in final products with small surface areas and non-porous structures.

#### 4.2.3. Hybrid Na-Air Batteries

Except Li–O<sub>2</sub> batteries, Abirami et al also used porous spinel-type cobalt manganese oxide (CMO) nanocubes derived from PBA-MnCo in a hybrid Na–Air/seawater battery.<sup>[101]</sup> The hybrid battery consists of an air-cathode in an alkaline electrolyte, a Na anode in an organic electrolyte, and a Na superionic conductor (NASICON) ceramic electrolyte between them. During the charge process, the Na<sup>+</sup> ions were reduced to metallic Na by transporting from the seawater to the anode section through the NASICON separator, and the OER occurred simultaneously at the cathode. While in discharge process, the metallic Na is oxidized to Na<sup>+</sup> at the anode, which moves into the seawater to form soluble NaOH with ORR product.<sup>[101]</sup> As the schematic in Figure 11a, the cubic PBA-MnCo was annealed in air to produce the porous CMO nanocubes which exhibits the XRD patterns of (Co,Mn)(CoMn)<sub>2</sub>O<sub>4</sub> (PDF No. 18-0408, JCPDS) with tetragonal spinel structure. Due to the similar chemical states, ionic radii

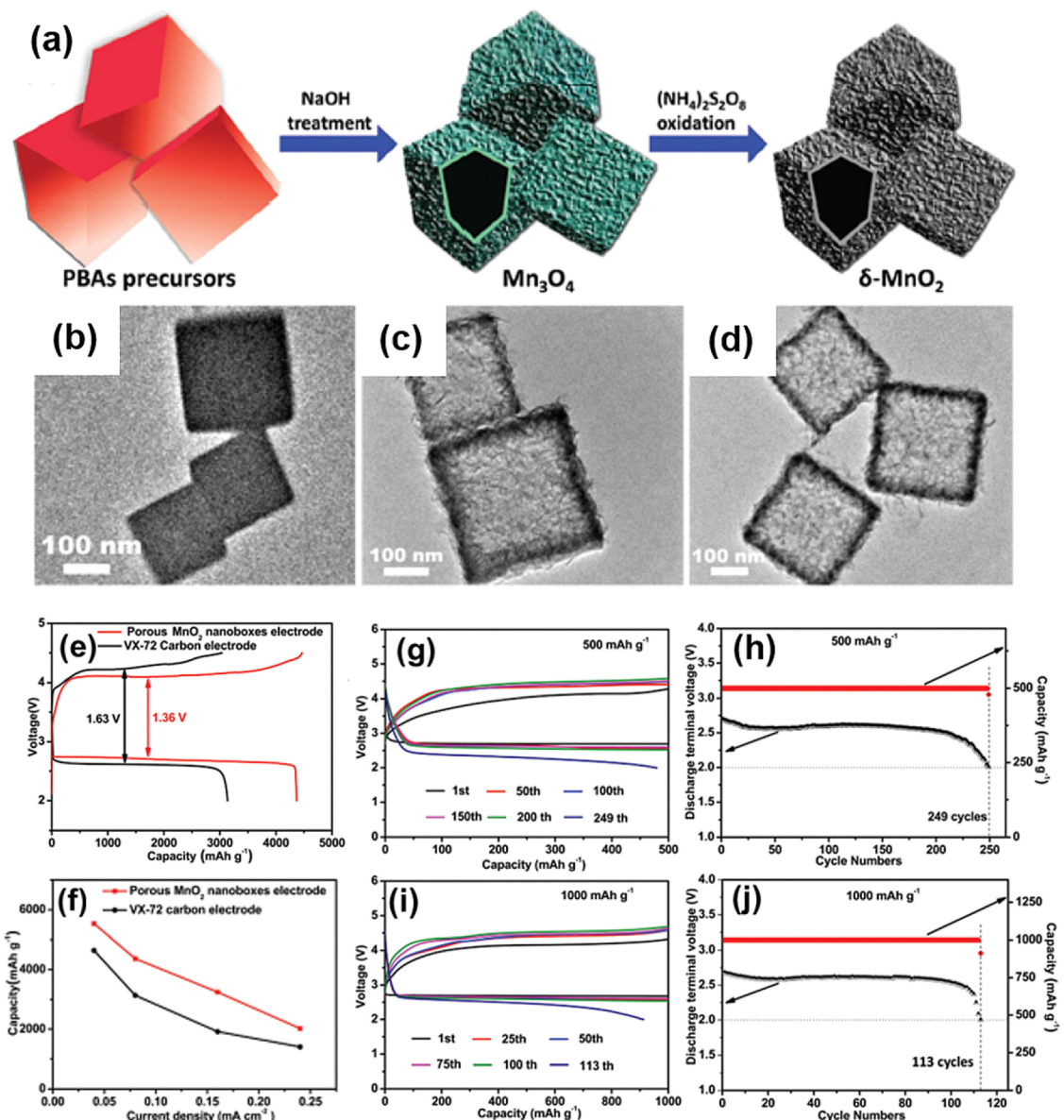


**Figure 10.** (a) Schematic illustration of the formation of the hierarchical porous δ-MnO<sub>2</sub> nanoboxes. (b) TEM images of the obtained nanocube-like PBA precursors, (c) porous Mn<sub>3</sub>O<sub>4</sub> nanoboxes and (d) hierarchical porous δ-MnO<sub>2</sub> nanoboxes. (e) First discharge-charge curves of Li–O<sub>2</sub> batteries with the hierarchical porous δ-MnO<sub>2</sub> nanoboxes and VX-72 carbon electrodes at 0.08 mA cm<sup>-2</sup>; (f) discharge capacity of Li–O<sub>2</sub> battery cells with different electrodes at various current densities; (g–j) Cyclic performance of a hierarchical porous δ-MnO<sub>2</sub> nanobox electrode at 0.16 mA cm<sup>-2</sup> with limited capacity of 500 mA h g<sup>-1</sup> (g and h) and 1000 mA h g<sup>-1</sup> (i and j), respectively.<sup>[99]</sup> Reprinted (adapted) with permission from ref. 99. Copyright (2015) The Royal Society of Chemistry.

and miscibility of each elements, the Co and Mn cations randomly distributed in the octahedral and tetrahedral sites of (Co,Mn)(CoMn)<sub>2</sub>O<sub>4</sub> phase.<sup>[102]</sup> By calculating the deconvoluted XPS data, they found the surface of the porous CMO nanocubes had average oxidation states of +2.69 for Mn and +2.46 for Co, which plays a positive role in guaranteeing the bifunctional catalytic property via balancing the ORR and OER activities.<sup>[102,103]</sup> Additionally, the XPS qualitative measurements reveal the CMO nanocubes have a Mn-rich surface structure ascribed to the higher outward diffusion rate of Mn cations than Co cations during the heat treatment.<sup>[104]</sup> Figure 11g compares the profiles of initial charge-discharge voltage of cells employing different electrocatalysts under the current density

of 0.01 mA cm<sup>-2</sup> for 20 h. Obviously, the cell using the CMO-loaded carbon paper exhibited the best electrochemical behaviour with a small voltage gap ( $\Delta V$ ) of 0.53 V compared to that of the cells using commercial Pt/C (~0.64 V) and Ir/C (~0.73 V) nanoparticles. Besides, the CMO cell also shows a good cycle stability after 30 cycles with the average charge/discharge voltages of ~3.58/~3.05 V, respectively, attaining a high voltage efficiency of ~85% (Figure 11g–11i). Furthermore, when replacing the Na anode with a hard carbon, the Na-metal-free seawater battery displayed a good cycle performance as well with an average discharge voltage of ~2.7 V and a discharge capacity of ~190 mA h g<sup>-1</sup> (Figure 11j–11l). During 100 cycles, the full-cell exhibited a stable cycling performance with high

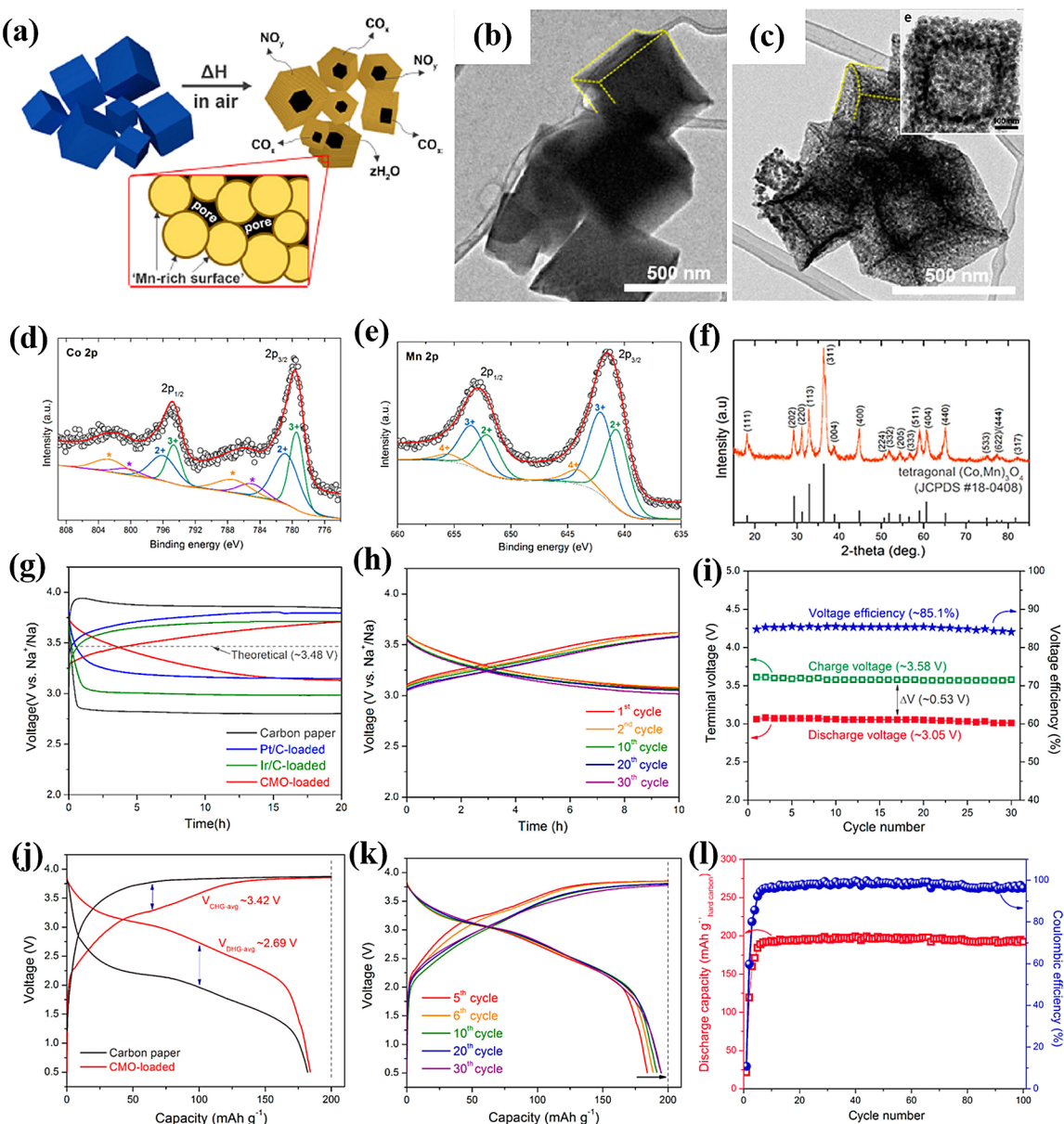


**Figure 11.** (a) A schematic illustration showing the morphological evolution of porous CMO nanocubes by air-annealing. (b–c) TEM images of (b) as-prepared Mn<sub>3</sub>[Co(CN)<sub>6</sub>]<sub>2</sub> nanocubes and (c) porous CMO nanocubes. (d) XRD pattern of porous CMO. XPS spectra of (e) Co 2p and (f) Mn 2p. (g) Initial charge-discharge voltage profiles of a seawater battery (Na/seawater) with different electrocatalysts at a current density of 0.01 mA cm<sup>-2</sup>; (h) charge-discharge curves (cycle performance) of a seawater battery with the CMO catalyst during 30 cycles, and (i) the terminal voltages and voltage efficiency during cycling. (j) Charge-discharge voltage profiles of the full-cells (hard carbon/seawater) with/without the CMO catalyst at the fifth cycle at a current rate of 0.01 mA cm<sup>-2</sup> and (k) the full-cell with respect to cycle number at 0.01 mA cm<sup>-2</sup>. (l) Variations of the discharge capacity and Coulombic efficiency of the full-cell with cycle number to 100 cycles.<sup>[101]</sup> Reprinted (adapted) with permission from ref. 101. Copyright (2016) American Chemical Society.

coulombic efficiencies beyond 96% and high energy efficiencies between 74–79%. Through analysing the XRD and XPS of the CMO catalysts after cycles, they revealed that no obvious changes were observed in the phase and surface electronic states, suggesting the durability of the CMO in this hybrid seawater battery. In a word, this improved performance was owing to the large surface area providing rich active sites and the high oxidation states in the CMO originating from the randomly distributed Co and Mn cations.

## 5. Conclusion and Perspective

This review summarizes the recent progress in the synthesis of different transition metal-based materials derived from PB/PBAs and highlights their performance for electrochemical reactions and application in metal-air batteries. In particular, PB/PBAs themselves can work directly as promising catalysts for ORR or OER owing to their unique compositions with metal sites and functional ligands, but their application are limited by their low conductivity and poor chemical stability. On account of the low cost, easy preparation, open-framework structure and tuneabil-

ity, PB/PBAs are suitable precursors for diverse transition metal-based nanocomposites in comparison with other MOFs.

As shown in Figure 12, the synthetic strategies to fabricate different materials derived from PB/PBAs for OER and ORR are concluded in the diagram. Thanks to the existence of –CN group and metal ions, the composites with core-shell structure can be easily obtained via directly carbonization of PB/PBA in inert atmosphere. And the resulted materials always show superior activity in both OER and ORR by reason of the rich N-dopants, multiple compositions and structure features. Similarly, this carbonization method is feasible in other MOFs as well. While they have more possibility to encapsulate various small molecules for additional functionalities or as templates to various porous catalysts and even single atom catalysts because the large organic linkers endowing them large pore sizes and interstitial space.<sup>[105–107]</sup> As comparison, PB and PBA have small unit cell with the –CN group easily evaporated during calcination, resulting in derived materials preferable to be aggregated together with large crystal size, which limits the final performance in some degree. Even though methods have been adopted to blend PB/PBAs with other carbon substrate to prevent the aggregation, it is still hard to precisely control the uniformity of crystal size and dispersion. Thus, controlling the growth of PB/PBA crystals at the beginning is significant for future study, which can broaden the availability of PB/PBA precursors. Although PB/PBA have no advantage to synthesis small metallic clusters and single atom catalysts, they are capable to different porous oxides and hydroxides by virtue of the release of –CN at low temperature and ion exchange with hexacyanometalate in alkaline condition. Besides, they are also excellent templates to various TMPs/TMSs or even transition-metal phosphorus trisulfide ( $\text{TMPS}_3$ ) through reacting with

corresponding vapours.<sup>[108,109]</sup> In this case, carefully controlling annealing temperatures and solvent concentration to engineer the surface composition and morphology are highly desirable.

Although we have witnessed significant advances in the synthesis of different materials from PB/PBAs with controllable particle size, morphology and compositions through facile approaches, their appealing applications in metal-air batteries remain many challenges. Firstly, chemical combinations make it difficult to comprehensively understand the real correlation of performance to each component, and it is also hard to explore the intrinsic activity of every single component in real experimental works. In this regard, calculation and modelling studies should be carried out to forecast the function of each substance, revealing the application potentials and property trends of specific material among numerous compositions. Additionally, constructing well-organized hierarchical porous architecture is important as well to improve the performance of batteries in practice since ORR/OER are gas-involving tri-phase reactions which are largely affected by the speed of mass transfer and ion exchange. At present, most of reported works are still concentrating on the optimization of compositions to improve the activity in ideal testing conditions but ignoring the architectures. Hence, more works can be developed to design bifunctional electrocatalysts from PBAs and other MOFs with proper architecture or adjust the hydrophobicity/hydrophilicity of catalyst surface to accelerate mass transport in metal-air batteries.

In this work, we show the possibility of PB/PBAs as good precursors to various active materials for ORR and OER by complete collapse of the frameworks. However, we disregard the merit of high ordering and dispersion of the metal sites in framework-structured catalyst. Although previous studies show

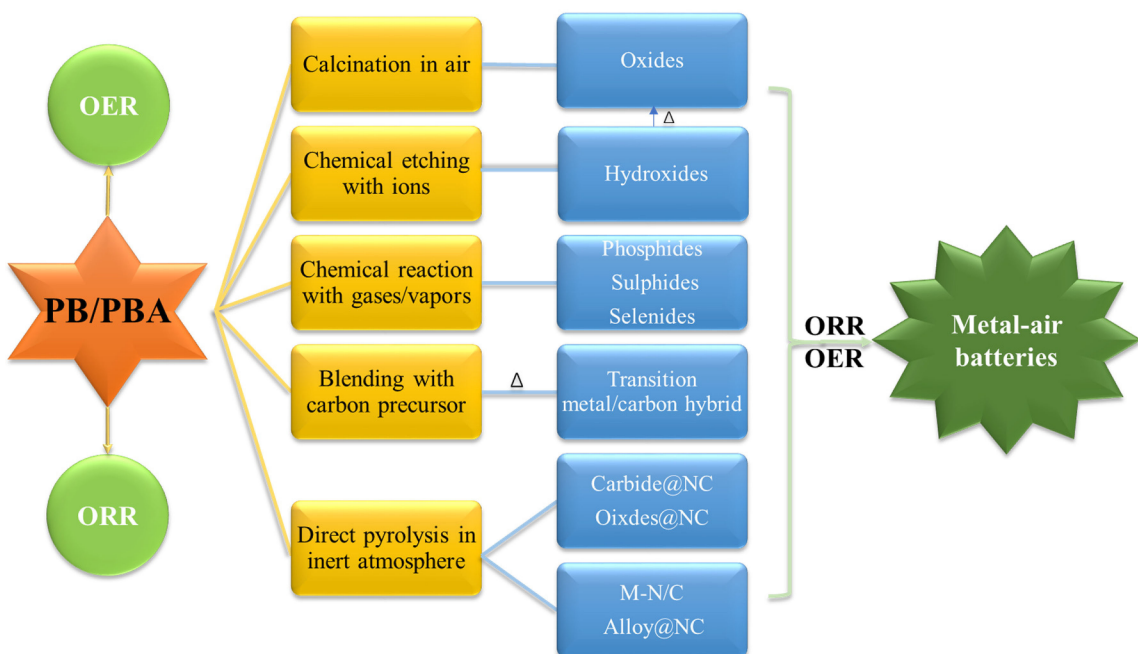


Figure 12. An overview of the synthetic strategies of PB/PBA-derived nanocatalysts and use for metal-air battery.

PB/PBAs have low stability and limited activity, we can use other methods to activate the metal sites or modify them in a framework to improve the activity and the stability. For example, low-temperature air plasma have been used to active the PBA without destroying the cubic framework.<sup>[110]</sup> This method can also be expanded into other MOFs. All in all, the rapid development of PB/PBA and other MOF-based materials have driven the development of energy storage and conversion device quickly. With continuous efforts devoted, it is believed that the fundamental studies on MOFs themselves are still required in order to accelerate their practical usage for highly efficient electrochemical energy-related applications.

## Acknowledgement

The authors thank the financial support from the Australian Research Council Discovery Project (DP160103244), the UNSW Faculty of Engineering Start-up grant and the UNSW-SJTU seed grant.

## Conflict of Interest

The authors declare no conflict of interest.

**Keywords:** meta-air batteries • oxygen electrocatalyst • Prussian blue • Prussian blue analogues

- [1] M. Z. Jacobson, M. A. Delucchi, *Energy Policy* **2011**, *39*, 1154–1169.
- [2] M. Armand, J.-M. Tarascon, *Natur* **2008**, *451*, 652–657.
- [3] Y. Zhao, Z. Song, X. Li, Q. Sun, N. Cheng, S. Lawes, X. Sun, *Energy Storage Mater.* **2016**, *2*, 35–62.
- [4] Y. Wang, Y. Song, Y. Xia, *Chem. Soc. Rev.* **2016**, *45*, 5925–5950.
- [5] M. Winter, R. J. Brodd, *Chem. Rev.* **2004**, *104*, 4245–4270.
- [6] M. S. Islam, C. A. J. Fisher, *Chem. Soc. Rev.* **2014**, *43*, 185–204.
- [7] X. Zuo, J. Zhu, P. Müller-Buschbaum, Y.-J. Cheng, *Nano Energy* **2017**, *31*, 113–143.
- [8] G. E. Blomgren, *J. Electrochem. Soc.* **2017**, *164*, A5019–A5025.
- [9] X. Feng, M. Ouyang, X. Liu, L. Lu, Y. Xia, X. He, *Energy Storage Mater.* **2018**, *10*, 246–267.
- [10] M. A. Hannan, M. S. H. Lipu, A. Hussain, A. Mohamed, *Renewable Sustainable Energy Rev.* **2017**, *78*, 834–854.
- [11] X. Yao, Q. Dong, Q. Cheng, D. Wang, *Angew. Chem. Int. Ed.* **2016**, *55*, 11344–11353; *Angew. Chem.* **2016**, *128*, 11514–11524.
- [12] X. Y. Yu, X. W. (David) Lou, *Adv. Energy Mater.* **2018**, *8*, 1–37.
- [13] Y. Li, J. Lu, *ACS Energy Lett.* **2017**, *2*, 1370–1377.
- [14] H. Wang, Q. L. Zhu, R. Zou, Q. Xu, *Chem* **2017**, *2*, 52–80.
- [15] L. Grande, E. Paillard, J. Hassoun, J.-B. Park, Y.-J. Lee, Y.-K. Sun, S. Passerini, B. Scrosati, *Adv. Mater.* **2015**, *27*, 784–800.
- [16] Z.-L. Wang, D. Xu, J.-J. Xu, X.-B. Zhang, *Chem. Soc. Rev.* **2014**, *43*, 7746–7786.
- [17] Z. Zhao, M. Li, L. Zhang, L. Dai, Z. Xia, *Adv. Mater.* **2015**, *27*, 6834–6840.
- [18] R. D. McKerracher, C. Ponce de Leon, R. G. A. Wills, A. A. Shah, F. C. Walsh, *ChemPlusChem* **2015**, *80*, 323–335.
- [19] E. Davari, D. Ivey, *Sustain. Energy Fuels* **2018**, *2*, 39–67.
- [20] D. Gelman, B. Shvartsev, Y. Ein-Eli, *J. Mater. Chem. A* **2014**, *2*, 20237–20242.
- [21] Q. Liu, Z. Chang, Z. Li, X. Zhang, *Small Methods* **2018**, *2*, 1700231.
- [22] P. Reinsberg, C. J. Bondue, H. Baltruschat, *J. Phys. Chem. C* **2016**, *120*, 22179–22185.
- [23] G. Toussaint, P. Stevens, L. Akrou, R. Rouget, F. Fourgeot, *ECS Trans.* **2010**, *28*, 25–34.
- [24] Y. Li, H. Dai, *Chem. Soc. Rev.* **2014**, *43*, 5257–5275.
- [25] W. Chen, Y. F. Gong, J. H. Liu, *Chinese Chem. Lett.* **2017**, *28*, 709–718.
- [26] Y. Qian, I. A. Khan, D. Zhao, *Small* **2017**, *13*, 1701143.
- [27] G. Fu, Y. Tang, J. M. Lee, *ChemElectroChem* **2018**, *5*, 1424–1434.
- [28] H. Osgood, S. V. Devaguptapu, H. Xu, J. Cho, G. Wu, *Nano Today* **2016**, *11*, 601–625.
- [29] G. Wu, A. Santandreu, W. Kellogg, S. Gupta, O. Ogoke, H. Zhang, H. L. Wang, L. Dai, *Nano Energy* **2016**, *29*, 83–110.
- [30] X. Cui, S. Yang, X. Yan, J. Leng, S. Shuang, P. M. Ajayan, Z. Zhang, *Adv. Funct. Mater.* **2016**, *26*, 5708–5717.
- [31] Y. J. Sa, D. J. Seo, J. Woo, J. T. Lim, J. Y. Cheon, S. Y. Yang, J. M. Lee, D. Kang, T. J. Shin, H. S. Shin, *J. Am. Chem. Soc.* **2016**, *138*, 15046–15056.
- [32] A. Paolella, C. Faure, V. Timochevskii, S. Marras, G. Bertoni, G. Abdelbast, A. Vijh, M. Armand, K. Zaghib, *J. Mater. Chem. A* **2017**, *5*, 18919–18932.
- [33] W. Zhang, Y. Zhao, V. Malgras, Q. Ji, D. Jiang, R. Qi, K. Ariga, Y. Yamauchi, J. Liu, J. Sen Jiang, *Angew. Chem. Int. Ed.* **2016**, *55*, 1–7; *Angew. Chem.* **2016**, *128*, 1–1.
- [34] Y. Song, J. He, H. Wu, X. Li, J. Yu, Y. Zhang, L. Wang, *Electrochim. Acta* **2015**, *182*, 165–172.
- [35] C. D. Wessells, R. a Huggins, Y. Cui, *Nat. Commun.* **2011**, *2*, 550.
- [36] X. J. Wang, F. Krumeich, R. Nesper, *Electrochim. Commun.* **2013**, *34*, 246–249.
- [37] L. Xu, G. Zhang, J. Chen, G. Yuan, L. Fu, F. Yang, *J. Inst. Chem.* **2016**, *58*, 374–380.
- [38] B. Kong, C. Selomulya, G. Zheng, D. Zhao, *Chem. Soc. Rev.* **2015**, *44*, 7997–8018.
- [39] L. Li, Z. Chang, X.-B. Zhang, *Adv. Sustain. Syst.* **2017**, *1*, 1700036.
- [40] Y. Jiao, Y. Zheng, M. Jaroniec, S. Z. Qiao, *Chem. Soc. Rev.* **2015**, *44*, 2060–2086.
- [41] Z. F. Huang, J. Wang, Y. Peng, C. Y. Jung, A. Fisher, X. Wang, *Adv. Energy Mater.* **2017**, *7*, 1700544.
- [42] Z. W. She, J. Kibsgaard, C. F. Dickens, I. Chorkendorff, J. K. Nørskov, T. F. Jaramillo, *Science* **2017**, *355*, eaad4998.
- [43] J.-X. Feng, S.-H. Ye, H. Xu, Y.-X. Tong, G.-R. Li, *Adv. Mater.* **2016**, *28*, 4698–4703.
- [44] X.-F. Lu, L.-F. Gu, J.-W. Wang, J.-X. Wu, P.-Q. Liao, G.-R. Li, *Adv. Mater.* **2017**, *29*, 1604437.
- [45] H. A. Gasteiger, N. M. Marković, H. A. Gasteiger, J. B. Goodenough, Y. Shao-Horn, *Science* **2009**, *324*, 48–9.
- [46] M. S. Burke, L. J. Enman, A. S. Batchellor, S. Zou, S. W. Boettcher, *Chem. Mater.* **2015**, *27*, 7549–7558.
- [47] A. Kraytsberg, Y. Ein-Eli, *Nano Energy* **2013**, *2*, 468–480.
- [48] S. Dou, X. Wang, S. Wang, *Small Methods* **2018**, 1800211.
- [49] J. Nai, X. W. D. Lou, *Adv. Mater.* **2018**, 1706825.
- [50] H. Zhang, J. Nai, L. Yu, X. W. (David) Lou, *Joule* **2017**, *1*, 77–107.
- [51] K. Itaya, N. Shoji, I. Uchida, *J. Am. Chem. Soc.* **1984**, *106*, 3423–3429.
- [52] L. Xu, G. Zhang, J. Chen, Y. Zhou, G. Yuan, F. Yang, *J. Power Sources* **2013**, *240*, 101–108.
- [53] J. Sanetuntikul, S. Shanmugam, *Electrochim. Acta* **2014**, *119*, 92–98.
- [54] P. Zhang, X. Wang, W. Wang, X. Lei, H. Yang, *RSC Adv.* **2015**, *5*, 21670–21674.
- [55] M. Xiao, J. Zhu, L. Feng, C. Liu, W. Xing, *Adv. Mater.* **2015**, *27*, 2521–2527.
- [56] J. Wei, Y. Liang, Y. Hu, B. Kong, G. P. Simon, J. Zhang, S. P. Jiang, H. Wang, *Angew. Chem. Int. Ed.* **2016**, *55*, 1355–1359; *Angew. Chem.* **2016**, *128*, 1377–1381.
- [57] M. B. Zakaria, *RSC Adv.* **2016**, *6*, 10341–10351.
- [58] Y. Hou, T. Huang, Z. Wen, S. Mao, S. Cui, J. Chen, *Adv. Energy Mater.* **2014**, *4*, 1400337.
- [59] Y. Liu, H. Wang, D. Lin, J. Zhao, C. Liu, J. Xie, Y. Cui, *Nano Res.* **2017**, *10*, 1213–1222.
- [60] X. Wang, L. Zou, H. Fu, Y. Xiong, Z. Tao, J. Zheng, X. Li, *ACS Appl. Mater. Interfaces* **2016**, *8*, 8436–8444.
- [61] D. Zhao, L. Li, L. Xie, N. Zhou, S. Chen, *J. Alloys Compd.* **2018**, *741*, 368–376.
- [62] L. Du, L. Luo, Z. Feng, M. Engelhard, X. Xie, B. Han, J. Sun, J. Zhang, G. Yin, C. Wang, *Nano Energy* **2017**, *39*, 245–252.
- [63] A. Sivanantham, P. Ganeshan, L. Estevez, B. P. McGrail, R. K. Motkuri, S. Shanmugam, *Adv. Energy Mater.* **2018**, *8*, 1702838.
- [64] L. Han, X. Y. Yu, X. W. D. (David) Lou, *Adv. Mater.* **2016**, *28*, 4601–4605.
- [65] Y. Feng, X. Yu, U. Paik, *Chem. Commun.* **2016**, *52*, 6269–6272.
- [66] V. Ganesan, J. Kim, *Mater. Lett.* **2018**, *223*, 49–52.
- [67] X. Y. Yu, L. Yu, H. Bin Wu, X. W. Lou, *Angew. Chem. Int. Ed.* **2015**, *54*, 5331–5335; *Angew. Chem.* **2015**, *127*, 5421–5425.

- [68] L. Zhang, H. Bin Wu, X. W. Lou, *J. Am. Chem. Soc.* **2013**, *135*, 10664–10672.
- [69] J. Nai, X. W. Lou, *Adv. Mater.* **2018**, 1706825.
- [70] P. Cai, J. Huang, J. Chen, Z. Wen, *Angew. Chem.* **2017**, *129*, 4936–4939; *Angew. Chem. Int. Ed.* **2017**, *56*, 4858–4861.
- [71] L.-A. Stern, L. Feng, F. Song, X. Hu, *Energy Environ. Sci.* **2015**, *8*, 2347–2351.
- [72] X. Yu, Y. Feng, B. Guan, X. W. D. Lou, U. Paik, *Energy Environ. Sci.* **2016**, *9*, 1–16.
- [73] Z. Chen, R. Wu, M. Liu, Y. Liu, S. Xu, Y. Ha, Y. Guo, X. Yu, D. Sun, F. Fang, *J. Mater. Chem. A* **2018**, *6*, 10304–10312.
- [74] S. Pintado, S. Goberna-ferro, E. C. Escudero-ada, S. Goberna-Ferrón, E. C. Escudero-Adán, J. R. Galán-Mascarós, *J. Am. Chem. Soc.* **2013**, *135*, 13270–13273.
- [75] L. Han, P. Tang, A. Reyes-Carmona, B. Rodriguez-Garcia, M. Torrens, J. R. Morante, J. Arbiol, J. R. Galan-Mascaros, *J. Am. Chem. Soc.* **2016**, *138*, 16037–16045.
- [76] A. Indra, U. Paik, T. Song, *Angew. Chem. Int. Ed.* **2018**, *57*, 1241–1245; *Angew. Chem.* **2018**, *130*, 1255–1259.
- [77] C. Guo, Y. Zheng, J. Ran, F. Xie, M. Jaroniec, S. Z. Qiao, *Angew. Chem. Int. Ed.* **2017**, 8539–8543.
- [78] M. Q. Wang, C. Ye, M. Wang, T. H. Li, Y. N. Yu, S. J. Bao, *Energy Storage Mater.* **2018**, *11*, 112–117.
- [79] S. Ci, S. Mao, Y. Hou, S. Cui, H. Kim, R. Ren, Z. Wen, J. Chen, *J. Mater. Chem. A* **2015**, *3*, 7986–7993.
- [80] S. Gadipelli, T. Zhao, S. A. Shevlin, Z. Guo, *Energy Environ. Sci.* **2016**, *9*, 1661–1667.
- [81] B. K. Barman, K. K. Nanda, *Green Chem.* **2016**, *18*, 427–432.
- [82] L. Lai, J. R. Potts, D. Zhan, L. Wang, C. Kok, C. Tang, H. Gong, Z. Shen, J. Lin, R. S. Ruoff, *Energy Environ. Sci.* **2012**, *5*, 7936–7942.
- [83] J. Su, G. Xia, R. Li, Y. Yang, J. Chen, R. Shi, P. Jiang, Q. Chen, *J. Mater. Chem. A* **2016**, *4*, 9204–9212.
- [84] Z. Shang, Z. Chen, Z. Zhang, J. Yu, S. Tan, F. Ciucci, Z. Shao, H. Lei, D. Chen, *J. Alloys Compd.* **2018**, *740*, 743–753.
- [85] X. Li, L. Yuan, J. Wang, L. Jiang, A. I. Rykov, D. L. Nagy, C. Bogdán, M. A. Ahmed, K. Zhu, G. Sun, *Nanoscale* **2016**, *8*, 2333–2342.
- [86] X. Wang, X. Liu, C.-J. Tong, X. Yuan, W. Dong, T. Lin, L.-M. Liu, F. Huang, *J. Mater. Chem. A* **2016**, *4*, 7762–7771.
- [87] S. Gupta, L. Qiao, S. Zhao, H. Xu, Y. Lin, S. V. Devaguptapu, X. Wang, M. T. Swihart, G. Wu, *Adv. Energy Mater.* **2016**, *6*, 1601198.
- [88] M. Zeng, Y. Liu, F. Zhao, K. Nie, N. Han, X. Wang, W. Huang, X. Song, J. Zhong, Y. Li, *Adv. Funct. Mater.* **2016**, *26*, 4397–4404.
- [89] Y. Li, M. Gong, Y. Liang, J. Feng, J.-E. Kim, H. Wang, G. Hong, B. Zhang, H. Dai, *Nat. Commun.* **2013**, *4*, 1805.
- [90] G. Nam, J. Park, M. Choi, P. Oh, S. Park, M. G. Kim, N. Park, J. Cho, J.-S. Lee, *ACS Nano* **2015**, *9*, 6493–6501.
- [91] J. S. Lee, G. Nam, J. Sun, S. Higashi, H. W. Lee, S. Lee, W. Chen, Y. Cui, J. Cho, *Adv. Energy Mater.* **2016**, *6*, 1601052.
- [92] J. Yang, J. Hu, M. Weng, R. Tan, L. Tian, J. Yang, J. Amine, J. Zheng, H. Chen, F. Pan, *ACS Appl. Mater. Interfaces* **2017**, *9*, 4587–4596.
- [93] P. Cai, S. Ci, E. Zhang, P. Shao, C. Cao, Z. Wen, *Electrochim. Acta* **2016**, *220*, 354–362.
- [94] D. Wang, X. Chen, D. G. Evans, W. Yang, *Nanoscale* **2013**, *5*, 5312–5.
- [95] L. Wang, C. Lin, D. Huang, F. Zhang, M. Wang, J. Jin, *ACS Appl. Mater. Interfaces* **2014**, *6*, 10172–10180.
- [96] R. D. L. Smith, M. S. Prévôt, R. D. Fagan, Z. Zhang, P. A. Sedach, M. K. J. Siu, S. Trudel, C. P. Berlinguet, *Science* **2013**, *340*, 60–3.
- [97] L. Wei, H. E. Karahan, S. Zhai, H. Liu, X. Chen, Z. Zhou, Y. Lei, Z. Liu, Y. Chen, *Adv. Mater.* **2017**, *29*, 1701410.
- [98] L. Hu, P. Zhang, H. Zhong, X. Zheng, N. Yan, Q. Chen, *Chem. Eur. J.* **2012**, *18*, 15049–15056.
- [99] J. Zhang, Y. Luan, Z. Lyu, L. Wang, L. Xu, K. Yuan, F. Pan, M. Lai, Z. Liu, W. Chen, *Nanoscale* **2015**, *7*, 14881–14888.
- [100] J. Zhang, Z. Lyu, F. Zhang, L. Wang, P. Xiao, K. Yuan, M. Lai, W. Chen, *J. Mater. Chem. A* **2016**, *4*, 6350–6356.
- [101] M. Abirami, S. M. Hwang, J. Yang, S. T. Senthilkumar, J. Kim, W.-S. Go, B. Senthilkumar, H.-K. Song, Y. Kim, *ACS Appl. Mater. Interfaces* **2016**, *8*, 32778–32787.
- [102] J. Zhang, L. Wang, L. Xu, X. Ge, X. Zhao, M. Lai, Z. Liu, W. Chen, *Nanoscale* **2015**, *7*, 720–726.
- [103] X. Ge, Y. Liu, F. W. T. Goh, T. S. A. Hor, Y. Zong, P. Xiao, Z. Zhang, S. H. Lim, B. Li, X. Wang, *ACS Appl. Mater. Interfaces* **2014**, *6*, 12684–12691.
- [104] W. Wei, W. Chen, D. G. Ivey, *Chem. Mater.* **2008**, *20*, 1941–1947.
- [105] Q.-L. Zhu, W. Xia, L.-R. Zheng, R. Zou, Z. Liu, Q. Xu, *ACS Energy Lett.* **2017**, *2*, 504–511.
- [106] Y. Chen, S. Ji, Y. Wang, J. Dong, W. Chen, Z. Li, R. Shen, L. Zheng, Z. Zhuang, D. Wang, Y. Li, *Angew. Chem. Int. Ed.* **2017**, *56*, 6937–6941; *Angew. Chem.* **2017**, *129*, 7041–7045.
- [107] P. Yin, T. Yao, Y. Wu, L. Zheng, Y. Lin, W. Liu, H. Ju, J. Zhu, X. Hong, Z. Deng, G. Zhou, S. Wei, Y. Li, *Angew. Chem. Int. Ed.* **2016**, *55*, 10800–10805; *Angew. Chem.* **2016**, *128*, 10958–10963.
- [108] Z. Liu, Y. Wang, R. Chen, C. Chen, H. Yang, J. Ma, Y. Li, S. Wang, *J. Power Sources* **2018**, *403*, 90–96.
- [109] C. Xuan, J. Wang, W. Xia, J. Zhu, Z. Peng, K. Xia, W. Xiao, H. L. Xin, D. Wang, *J. Mater. Chem. A* **2018**, *6*, 7062–7069.
- [110] Y. Guo, T. Wang, J. Chen, J. Zheng, X. Li, K. (Ken) Ostrikov, *Adv. Energy Mater.* **2018**, *8*, 1–8.

Manuscript received: October 29, 2018

Revised manuscript received: January 8, 2019

Accepted manuscript online: January 8, 2019

Version of record online: February 5, 2019